OPEN ACCESS

University of BRISTOL

This electronic thesis or dissertation has been downloaded from Explore Bristol Research, http://research-information.bristol.ac.uk

Author:
Chen, Wenhan

Title:
GW calculations for Co2MnSi

General rights
Access to the thesis is subject to the Creative Commons Attribution - NonCommercial-No Derivatives 4.0 International Public License. A copy of this may be found at https://creativecommons.org/licenses/by-nc-nd/4.0/legalcode This license sets out your rights and the restrictions that apply to your access to the thesis so it is important you read this before proceeding.

Take down policy
Some pages of this thesis may have been removed for copyright restrictions prior to having it been deposited in Explore Bristol Research. However, if you have discovered material within the thesis that you consider to be unlawful e.g. breaches of copyright (either yours or that of a third party) or any other law, including but not limited to those relating to patent, trademark, confidentiality, data protection, obscenity, defamation, libel, then please contact collections-metadata@bristol.ac.uk and include the following information in your message:

• Your contact details
• Bibliographic details for the item, including a URL
• An outline nature of the complaint

Your claim will be investigated and, where appropriate, the item in question will be removed from public view as soon as possible.

GW calculations for Co_2MnSi

Wenhan Chen

A dissertation submitted to the University of Bristol in accordance with the requirements for award of the degree of Master of Science by research in the Faculty of Science

May 2019

Word count:18289

Abstract

The state-of-the-art GW approximation method has been used to discover the correlations of electrons in full Heusler alloy Co_2MnSi. Co_2MnSi has been studied as a candidate of spintronics devices due to its 100% spin-polarization at Fermi level. However, Co_2MnSi with transition metals also plays host to strong electron correlations which result in the difficulties of theoretical prediction with traditional DFT methods. Previous study shows that the Fermi surfaces of DFT-LSDA calculation are different from the Compton scattering experiments. The GW method that is based on Hedin's equations is designed to describe the self-energy which contains the complex exchange-correlation interactions beyond the DFT. A high-accuracy single-shot GW calculation is performed to reconstruct the Fermi surfaces of Co_2MnSi. From the results of GW calculation, the correlation problems have been significantly corrected which give a better description of the Fermi surfaces of Co_2MnSi. A combination of the GW method and the high-resolution Compton scattering technique provides a way to investigate the Fermi surfaces of strongly-correlated materials.

Acknowledgements

First and foremost, I would like to show my deepest gratitude to my supervisor, Prof. Stephen Dugdale, a respectable, responsible and resourceful scholar, who has patiently provided me with valuable guidance in every stage of my study. Without his enlightening instruction, impressive kindness and patience, I could not have completed my thesis. He has spent much time reading through each draft and help me to review the thesis. His keen and vigorous academic observation also enlightens me not only in this thesis but also in my future study. I shall extend my thanks to Dr. Arkadiy Davydov and other developers of Elk code. During the workshop in Germany, they had helped me to re-understand the DFT from a higher level. I'd like to thanks my current students Eddie Harris-Lee, Alyn James and Daniel Lagos Llaguno. With their beneficial advice, I could work more efficiently. Last but not the least, I'd like to express my gratitude to my parents who have always been helping me out of difficulties and supporting me without a word of complaint.

I declare that the work in this dissertation was carried out in accordance with the requirements of the University's Regulations and Code of Practice for Research Degree Programmes and that it has not been submitted for any other academic award. Except where indicated by specific reference in the text, the work is the candidate's own work. Work done in collaboration with, or with the assistance of, others, is indicated as such. Any views expressed in the dissertation are those of the author.

Name: Wenhan Chen **Date:** May 2019

List of Figures

List of Tables

Contents

1 Introduction

Predicting new materials' properties and understanding their physical essence has always been one of the most important areas in modern physics. With the establishment of quantum mechanics and the breakthrough in understanding atomic structure, electrons' behaviours in materials are seen as the key to the emergence of various phenomena in solids, from electrical conduction to superconductivity or the spin-Hall effect [2]. The reasons that lead to such different electronic structure are from the differences in the atoms that compose the solids and their spatial arrangement.

It was Drude who first use the concept of the electron to explain the properties of metals [3]. Used the approximation of classical mechanics which neglects all interactions of electrons and ions, he successfully predicted some properties which had been measured experimentally. After the establishment of quantum mechanics, the behaviours of particles such as electrons can be calculated directly with the Schrödinger equation. Thus, the description that is based on the Schrödinger equation and the Pauli principle result in the emergence of energy bands. Electrons as fermions are not allowed to occupy the same state with the same spin, so each band will be filled by only two electrons until all the electrons have been accommodated. The maximum energy of the occupied bands at zero temperature is the Fermi energy. The Fermi energy defines an interface between occupied states and unoccupied states, such an interface is called the Fermi surface which is the characteristic of metals [4].

From the Fermi-Dirac distribution, only the electrons that are close to the Fermi surface will be excited or scattered. Thus, research into the structure of Fermi surface has always been one of the most important parts of condensed matter physics. However, experimental measurement of Fermi surfaces is usually difficult and might be influenced by the defects of crystals. Traditional methods of

measuring the Fermi surface based on quantum oscillation like the de Haas-van Alphen (dHvA) effect, which requires very low temperatures in general [4]. A short introduction of experimental methods is discussed in Chapter 2 and Chapter 5.

Early theoretical prediction of Fermi surfaces was initially from the free electron model which is the quantum version of the Drude model. The Fermi surface of the free electron model is a sphere in momentum space, with a distinct change in the the occupation distribution of electrons at $k = k_F$. While for real materials in which the electrons are subject to a periodic potential, the Fermi surfaces will distort from the sphere-like simple model. In addition, a real material is in general composed of 10^{24} particles. It is impossible to solve the coupled Schrödinger equations for such a vast number of particles.

The well-known density functional theory (DFT) method was proposed by Kohn and Sham [5]. The DFT method uses the density of electrons $\rho(\boldsymbol{r})$ instead of the coordinates of each electron. It significantly reduces degrees of freedom of the studied problems from $3N$ to 3 [5]. In the past decades, DFT has became one of the most powerful tools for discovering the physical properties of solids, molecules and clusters. Much research has proved that DFT can provide an accurate result both qualitatively and quantitively [6]. However, DFT cannot capture all physics due to the poor approximations of exchange-correlation functionals [7]. Therefore DFT may be invalid on some special cases such as strongly correlated materials [8]. As a fundamental particle, correlations and exchange interactions between electrons make its behaviour more complicated. The widely used local density approximation(LDA) of the exchange-correlation functional is based on homogenous electron gas which neglects some important features of exchange-correlation interactions [5]. Thus, for some materials like the Heusler alloys, DFT-LDA calculation would give an inaccurate result [9].

Heusler alloys were found in last century by a German industrial metallurgist

[10]. It soon attracted much attention from physicists because consist of three non-magnetic elements but has magnetism. Besides its magnetism, a more exciting property from Slater-Pauling rule [11] is the half-metallicity of Heusler alloys. The majority spin electrons in Heusler alloys are metallic while the minority electrons are insulating or semiconducting which leads to 100% spin polarization at the Fermi level [12]. Consequently, Heusler alloys have been studied as candidates for spintronic devices.

A typical formula for full Heusler alloy is X_2YZ where X and Y are in general transition elements and Z is from the p-block. Therefore, d electrons in transition elements can make Heusler alloys play host to strong electron correlations which result in the difficulties of theoretical prediction with traditional DFT methods. An incorrect theoretical prediction of the Fermi surfaces of the Heusler alloy Co_2MnSi motivates us to find a better theory to describe the correlations between electrons in Co_2MnSi [9].

Several methods have been developed to solve the strongly correlated electron problem including the hybrid functionals, the DFT+U method and the GW method [13]. In this work, the GW method has been performed to correct the discrepancy between experiments and theory. The GW method is based on perturbative theory and designed to solve the Dyson equation which gives the connection between the Green's function and the self-energy [13]. It has been proved that with the description of the self-energy and quasi-particles, the predictions of electronic structures of materials could be significantly improved [14].

In chapter 5, a state-of-the-art GW calculation based on the Elk code was used to reconstruct the Fermi surfaces of Co_2MnSi. It successfully corrects the result that from standard DFT calculations and shows a very good agreement with the Compton scattering experiments. The structure of this dissertation will be organized as follows.

In chapter 2, the background theory of crystals and electronic structure will be discussed, where the concept of Fermi surface will be introduced. Besides the simple model, the Fermi liquid theory will be shortly discussed to provide a theoretical description of electron correlations which lead to the emergence of quasi-particles.

In chapter 3, the theoretical tool—DFT will be reviewed. The background of DFT—the Kohn-Sham equations and the Hohenberg-Kohen theorem will be discussed. Together with the widely used exchange-correlation functionals (the local density approximation (LDA) and the generalised gradient approximation (GGA)) [6], the numerical implementations of DFT will also be introduced in this chapter. In addition, the limitations of DFT will be presented at the end of chapter 3.

In chapter 4, the Green's function and GW theory will be discussed. The physical meaning of Green's function and its connection of eigenenergy and density of states will be introduced. The Hedin's equation, which is the theoretical foundation of GW method, will be introduced as well. In the last part of chapter 4, we will discuss how GW works in the ELK code. To show how the approach works, several simple materials will be calculated with GW method.

In chapter 5, a single-shot GW calculation is applied to the Heusler alloy Co_2MnSi. The DFT calculation and Compton scattering experiments of Co_2MnSi will be discussed briefly. The GW calculation of the Fermi surfaces of Co_2MnSi will be discussed in detailed to show the agreement between GW and the experiments.

All the results will be summarized in chapter 6.

2 Electrons in crystals

A crystalline solid is made up of massive ions and electrons. The number of particles in crystal is of the order of 10^{24}. As a consequence, describing the behaviour of these particles, especially the electrons, is an extremely difficult task. A key breakthrough was achieved by Laue in 1912 who first proved the existence of periodic structure in crystals with the technology of X-ray diffraction [15]. Based on his work, a minimal repeated cell can be extracted by setting an appropriate boundary condition. Such a repeated cell usually contains only several atoms. This gives us a possible way to study the properties of a limited number of particles in that cell, and these properties can be easily extended to the whole crystal. X-ray diffraction technology is still one of the most powerful tools for discovering the structure of crystals and other materials. Using the mathematical language used in X-ray diffraction, the concept of reciprocal space can be introduced naturally through the Fourier transform. In reciprocal space, some abstract properties can be visualized in a direct way, such as band structure and the Fermi surface of metals.

2.1 Periodic structure of crystals

A crystal is a kind of solid that has a periodic structure, described by an infinite array of discrete points—the Bravais lattice. Using this definition, a perfect crystal which has no defects and boundaries can be seen as the repetition of a primitive cell. In that sense, any point in the lattice can be expressed in real space coordinates with translation symmetry [16]:

$$R_l = l_1 \boldsymbol{a}_1 + l_2 \boldsymbol{a}_2 + l_3 \boldsymbol{a}_3, \tag{2.1}$$

where l_1, l_2, l_3 are integers, $\boldsymbol{a}_1, \boldsymbol{a}_2, \boldsymbol{a}_3$ are the basis vector of lattice. Seven crystal systems can be classified depending on the lengths and angles of these basis vectors. Further considering the differences of the positions of the lattice site, 14 Bravais lattice are formed which include all combinations of these positions. From the perspective of group theory, there are 32 point-groups and 230 space groups that represent all symmetry operations of macroscopic and microscopic symmetries. In addition, a special primitive cell can be chosen which has minimal volume. This cell usually called the Wigner-Seitz cell, which is formed by the planes that perpendicularly bisect each of the lattice vectors [16].

Although the real space description is an intuitive way to understand the periodic structures of crystalline lattices, it is not a good choice to study the electronic structure and many other properties of crystals (for example, phonons). As mentioned before, to discover these behaviours, a reciprocal space description is one of the most powerful mathematical tools. The correspondence between real space and reciprocal space can be written as:

$$\begin{aligned} \boldsymbol{b}_1 &= 2\pi \frac{\boldsymbol{a}_2 \times \boldsymbol{a}_3}{\boldsymbol{a}_1 \cdot [\boldsymbol{a}_2 \times \boldsymbol{a}_3]}, \\ \boldsymbol{b}_2 &= 2\pi \frac{\boldsymbol{a}_3 \times \boldsymbol{a}_1}{\boldsymbol{a}_1 \cdot [\boldsymbol{a}_2 \times \boldsymbol{a}_3]}, \\ \boldsymbol{b}_3 &= 2\pi \frac{\boldsymbol{a}_1 \times \boldsymbol{a}_2}{\boldsymbol{a}_1 \cdot [\boldsymbol{a}_2 \times \boldsymbol{a}_3]}, \end{aligned} \tag{2.2}$$

where $\boldsymbol{a}_1$, $\boldsymbol{a}_2$ and $\boldsymbol{a}_3$ are the basis vector in real space, $\boldsymbol{b}_1$, $\boldsymbol{b}_2$ and $\boldsymbol{b}_3$ are the corresponding basis vector in reciprocal space. Therefore:

$$\boldsymbol{a}_i \boldsymbol{b}_j = 2\pi \delta_{ij}, \tag{2.3}$$

where δ_{ij} is the Kronecker delta function. The lattice vector in reciprocal space is:

$$\boldsymbol{G} = h\boldsymbol{b_1} + k\boldsymbol{b_2} + l\boldsymbol{b_3}, \tag{2.4}$$

Obviously, symmetries of a crystal in real space has impacts on the symmetries in reciprocal space.

What is more, the Wigner-Seitz cell in reciprocal space can be also formed by same method as in real space. The Wigner-Seitz cell in reciprocal space is usually called the first Brillouin zone (BZ) which also has the minimum volume in reciprocal space.

2.2 Free electron model

It was J J Thomson who first discovered the electron as a fundamental particle in 1897 [17]. And not long after that, enlightened by the kinetic theory of gases, Drude proposed his classical model with this new particle to explain the physical properties of metals [3]. This hypothesis treats electrons as classical charged particles, where the electron-electron and electron-ion interactions are neglected. The scattering of the electrons is purely classical which follows a Poissonion process, meaning that the possibility of collision only depends on the relaxation time τ. At the first glance, the Drude model is a very rough approximation, but it successfully explains the problem of electrical conductivity, the Wiedemann-Franz law, the Hall effect and so on [16]. The quantum version of the free electron model was proposed by Sommerfeld in 1928. As in Drude's work, Sommerfeld also supposed that the Coulomb interactions between all particles can be neglected while the electron states are populated according to the Fermi-Dirac distribution. Under this premise, the multi-particle Schrödinger equation can be simplified to a

single-particle equation:

$$-\frac{\hbar^2}{2m}\nabla^2\psi(r) = E\psi(r) \tag{2.5}$$

To solve this equation, a suitable boundary condition must be considered. A real crystal has some finite size, but comparing the size of a primitive cell to that of a real crystal, it is reasonable to neglect the boundary effect if the studied primitive cell is located at the inner part of a macroscopic crystal. With this in mind, a special boundary condition which is called Born-von Kárman boundary condition can be introduced to solve the single particle Schrödinger Equation [16]. Under this condition, the wavefunction will satisfy:

$$\psi(\boldsymbol{r} + N_i\boldsymbol{a}_i) = \psi(\boldsymbol{r}), \tag{2.6}$$

where N_i is the number of primitive cells in the i dimension and $\boldsymbol{a}_i$ is the basis vector of i dimension. It is actually a cyclic condition which treats the crystal as a ring in each dimension. Consequently, the solution of the single-particle Schrödinger equation can be written as:

$$\psi(\boldsymbol{r}) = \frac{1}{\sqrt{V}}e^{ik\cdot r} \tag{2.7}$$

The corresponding eigenenergy is:

$$E(\boldsymbol{k}) = \frac{\hbar^2\boldsymbol{k}^2}{2m} \tag{2.8}$$

The energy distribution in k space is uniform thus the density of states can be written as:

$$D(E) = \frac{\delta N}{\delta E} = \frac{V}{2\pi^2}\left(\frac{2m}{\hbar^2}\right)^{3/2} E^{1/2} \tag{2.9}$$

The free electron model, from a modern point of view, is a very rough approximation which neglects all interactions between electrons and the lattice potential. But it still qualitatively gives some explanations of physical phenomena like Ohm's law. In addition, the shape of the density of states in energy space and the shape of the Fermi surface in k space also show some similar features with that in real crystals. The biggest problem of the free electron model is that it cannot explain the difference between conductors and insulators.

2.3 Bloch's theorem

As discussed before, owing to the periodic structure of crystals, together with Born-von Kárman boundary conditions, the translation symmetry is satisfied. Therefore, the solution of the Schrödinger equation with translational symmetry can be written as:

$$\psi(\boldsymbol{r} + \boldsymbol{R_n}) = \psi(\boldsymbol{r}), \tag{2.10}$$

where R_n is the lattice vector in real space. Bloch's theorem tells us that when the translation vector is some lattice vector, the change of wavefunction would only be a phase factor $e^{i\boldsymbol{k}\cdot\boldsymbol{R_n}}$. Thus, the wavefunction can be written as:

$$\psi(r) = e^{i\boldsymbol{k}\cdot\boldsymbol{R_n}} u(\boldsymbol{r}), \tag{2.11}$$

where $u(\boldsymbol{r})$ is a function that has same period as the lattice potential:

$$u(\boldsymbol{r}+\boldsymbol{R}) = u(\boldsymbol{r}) \tag{2.12}$$

This new wavefunction that is modulated with a function with the same periodicity as the lattice potential is called the Bloch function. The Bloch function can be written as a summation of Fourier seires as well [16]:

$$u_{\boldsymbol{k}}(\boldsymbol{r}) = \sum_{\boldsymbol{G}} a(\boldsymbol{k}+\boldsymbol{G}) e^{i\boldsymbol{G}\cdot\boldsymbol{r}}, \tag{2.13}$$

where $a(\boldsymbol{k}+\boldsymbol{G})$ is a Fourier coefficient. The Bloch function is directly derived from the lattice translation symmetry which is a property of crystals. Thus, the wavefunctions of electrons and other particles or quasi-particles in crystals can be also expressed with Bloch functions. In addition to this, it is noteworthy that if two wavevectors can be written as:

$$\boldsymbol{k} - \boldsymbol{k}' = \boldsymbol{G}_n, \tag{2.14}$$

where $\boldsymbol{G}_n$ is the basis vector of reciprocal lattice. Thus the phase factor is not unique:

$$\begin{aligned} e^{i\boldsymbol{k}\cdot\boldsymbol{R}_n} &= e^{i\boldsymbol{k}'\cdot\boldsymbol{R}_n} \cdot e^{i\boldsymbol{G}_n\cdot\boldsymbol{R}_n} \\ &= e^{i\boldsymbol{k}'\cdot\boldsymbol{R}_n} \end{aligned} \tag{2.15}$$

Consequently, the existence of the uncertainty of wavevector k indicates that the Bloch function is not a simultaneious eigenstate of both energy and momentum. This hints to us that the wavevector k must be constrained in some special volume where $\boldsymbol{k} - \boldsymbol{k}' \leq \boldsymbol{G}_n$. This special volume is the first BZ

2.4 Nearly free electron model

The free electron model assumes that the periodic lattice potential can be neglected and the electrons can be seen as free particles. If we further consider the fluctuation of periodic lattice potential as a perturbation, the free electron model becomes the nearly-free electron model:

$$\left[-\frac{\hbar^2}{2m}\nabla^2 + V(r)\right]\psi = E\psi, \tag{2.16}$$

$$\delta V(r) = V(r) - \overline{V}, \tag{2.17}$$

where $\overline{V}$ is the average potential in lattice and $\delta V(r)$ is the fluctuation of the periodical lattice potential. In the free electron model, the energy distribution in k space is a standard quadratic function. When the lattice potential pertubation is introduced, the energy distribution close to the boundary of first BZ will change significantly. The previous continuous distribution of energy is separated into two parts, the lower part that is completely or partly filled of electrons is the valence band while the higher part that is empty is called the conduction band. The forbidden area between the valence band and the conduction band is the band gap. The most important concept of the nearly free electron model is the band gap which successfully explains the essence of conductors and insulators. If an electron was excited by electrical field, an empty state was required. As an insulator, the valence bands are completely filled while the conduction bands are empty. The electrons in valence bands cannot move across the energy gap to the conduction gap. But for conductors, a partially filled band will allow electrons move freely.

2.4.1 Fermi surface

In the nearly-free electron model, electrons will fill the valence bands under the restrictions imposed by the Pauli principle. The distribution of electrons obeys the Fermi-Dirac distribution:

$$f(\varepsilon, T) = \frac{1}{e^{(\varepsilon-\varepsilon_F)/k_B T} + 1}, \tag{2.18}$$

where k_B is the Boltzmann constant and ε_F is the Fermi energy. A Fermi surface is defined as the interface of unoccupied states and occupied states in k space. If the temperature T is close to 0K, the Fermi-Dirac function will become a step function, and the occupied states and unoccupied states are separated by a very clear interface in k space. In that sense, it is obvious that the valence bands of insulators and semiconductors are completely filled while only metals have one or more partially filled bands that cross the Fermi level in first BZ. Therefore, a metal can be defined as a material with Fermi surface.

When it comes to finite temperature, the thermal electrons will slightly broaden the Fermi-Dirac function at the Fermi surface. Those occupied states above the Fermi energy come from the thermal excitation of electrons. In general, the typical value of Fermi energy of metals is 1—10eV which means that at room temperature, ε_F/k_bT is about 10^{-2}eV. Therefore, such broadening of the Fermi surface is very small which means that only those electrons very close to the Fermi surface will influence the thermal and electrical properties.

Different from the Fermi sphere in free electron model, the Fermi surface will be distorted at the boundary of first BZ due to the influence of the lattice potential in the nearly-free electron model. If one further considers the Coulomb interactions between electrons (within some approximations), the topology of Fermi surface is likely to be even more complex and is difficult to explain with simple models.

However, the topology of Fermi surface plays a very important role in explaining some behaviours of metals [4]. That requires us to develop some methods to discover the Fermi surface experimentally and theoretically.

To study the shape of Fermi surface, some of the most widely used experimental techniques are quantum oscillatory methods such as de Haas-van Alphen effect (dHvA) [18]. The quantization of electron orbits under the influence of a magnetic field can give information about the size of Fermi surface. In addition, photoemission can also be used to discover the Fermi surface [4]. Angle-resolved photoemission spectrum (ARPES) directly reveals the relation between the momentum and kinetic energy of photoelectrons and from the band dispersion, the shape of Fermi surface can be extracted. A disadvantage of ARPES is that it is surface sensitive [19]. Positron annihilation and Compton scattering experiments measure the momentum distribution of electrons, and are able to give the bulk information which can even be spin-resolved in some cases [20, 21]. A series of theoretical calculations that are based on DFT can also be used to discover the topology of Fermi surface. But due to the theoretical challenges of DFT and the unknown exchange-correlation functionals, it can be difficult to accurately predict the Fermi surfaces of complex alloys and d/f band metals accurately [8]. Another potential way that is based on Green's function theory like GW approximation, provides a novel solution of this problem. In this dissertation, we shall further see that the GW approximation, based on quasi-particle theory, will correct the discrepancy between DFT calculation and Compton scattering experiments.

2.4.2 Fermi liquid theory

It can be seen from the previous discussions that all simple models neglect the interaction between electrons. This is because the interactions between electrons in crystals are extremely difficult to be determined quantitatively. In a real multi-

electron system, the behaviour of a single electron is closely correlated with all the other 10^{23} electrons. An effective description of the weak excited states in an interacting system is known as Fermi liquid theory which was proposed by Landau in 1957 [22].

This theory starts from a non-interacting fermion system at low temperature. Landau assumes that the interaction between fermions can be introduced adiabatically and slowly. Such an assumption will lead to the emergence of quasi-particles which are formed by a group of states.

The quasi-particles can be seen as an electron that is 'dressed' with interactions with its environment. Each quasi-particle corresponds to a particle the in non-interacting system, which requires that they have same wavevector and spin. It actually indicates that the Fermi-Dirac distribution is also the distribution functions of quasi-particles. In contrast to the single-electron approximation, the total energy of the quasi-particles is no longer a simple summation of each quasi-particle, it now being the functional of the distribution of quasi-particles. This is because of the correlation effect of fermions.

With Landau's assumption, two conditions must be satisfied. A clear Fermi surface is necessary when describing the excited states of fermions. It requires that the distribution function $N(k)$ in k space satisfies [23]:

$$N(\boldsymbol{k}_F - 0) - N(\boldsymbol{k}_F + 0) = Z, \tag{2.19}$$

and

$$0 < Z \leq 1, \tag{2.20}$$

As shown in Figure **??** When $Z = 1$, the distribution function for the quasi-

particles becomes a step function which is the limit of a non-interacting electron gas. If $Z = 0$, Fermi liquid theory is invalid and the Fermi surface vanishes.

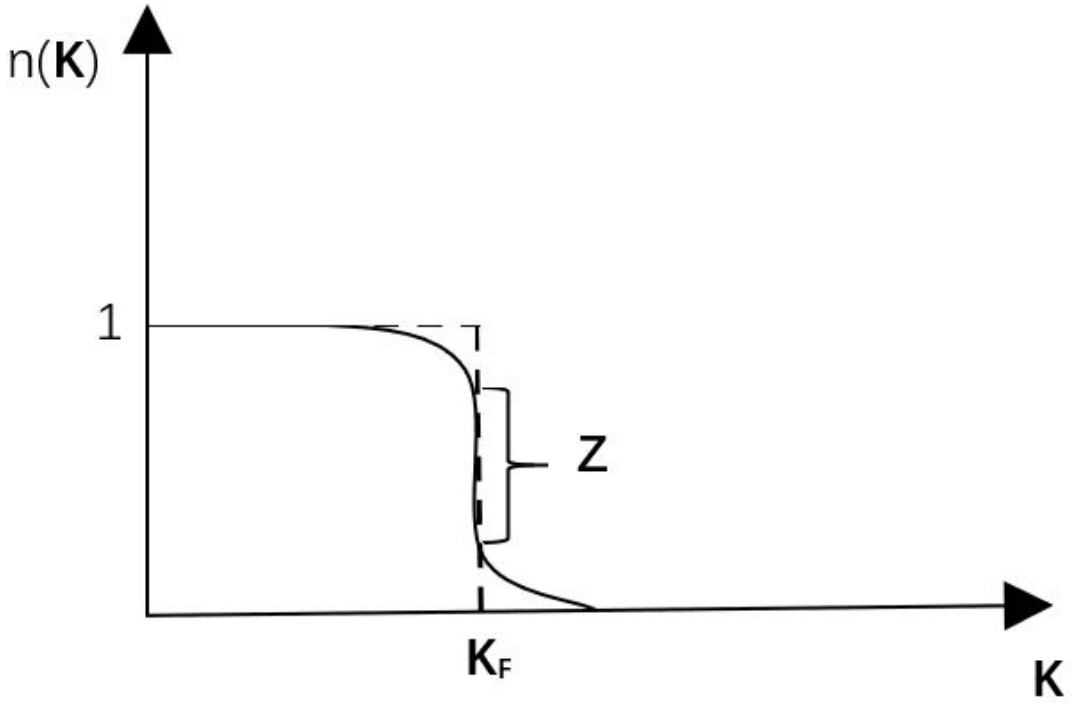

Figure 1: Illustration of Equation 2.20.

What is more, a quasi-particle is naturally required to have a relatively long life time. The life time τ can be roughly estimated by:

$$\tau \sim \frac{1}{(E - E_f)^2} \tag{2.21}$$

where E is the energy of quasi-particle, E_f is the Fermi energy. Considering the thermal excitation of quasi-particles close to Fermi surface, it actually requires that $k_B T \ll E_f$. Mathematically, Green's function $G(k, t)$ is the most powerful tool

to describe the behaviours of quasi-particles. By Fourier transforming withrespect to time, Green's functions can directly be used to calculate the spectra of quasi-particles. In Chapter 4, we will discuss this problem.

3 Density functional theory

The electronic structure is the key to understanding the behaviours of a solid material. The electronic structure gives a way of inferring the electromagnetic, optical and other properties of the materials. However, before the emergence of quantum mechanics, it was almost impossible to predict the properties of a new material crystal without any experiments. Therefore, discovering a new material was extremely inefficient and expensive. After Schrödinger's work, the behaviours of electrons in a material can be described with the Schrödinger equation in an accurate way. It had made a great progress in predicting the spectra of a single hydrogen atom. But for many electrons system even like helium, it is extremely difficult to be solved analytically [24]. For a real solid with 10^{23} atoms, an exact solution of such system is obviously impossible.

However, we still want to be able to predict the properties of complex solid crystals or molecules. In 1965, Kohn and Sham published their paper of solving this problem [5]. A functional of the electron density was used as the main variable of the studied system instead of the coordinates of the electrons, which greatly decreased the degrees of freedom of the all-electron Schrödinger equation. This became known as density functional theory (DFT). Considering the computer technology at that time, it was still difficult to apply it for a complex system.

In the following decades, with the rapid improvement of the power of computers, more and more scientists began to use DFT as their theoretical tool to understand and predict the properties of solid and molecules [6]. Although most of those calculated results show a very good agreement with experiments, the essential shortcomings of DFT and the approximation to the exchange-correlation functionals can make its predictions become invalid for some problems such as band gap problem of semiconductors or the strongly correlated problems [25].

3.1 Hohenberg-Kohn theorem

Within the Born-Oppenheimer approximation [26], an ion in a crystal can be seen as an object that is fixed at its position with the electrons moving in a periodic potential provided by the ion. In following chapters of this dissertation, atomic units will be used($\hbar = m_e = k_B = 1, c = 137$) to simplify the expression of equations. The Hamiltonian of this system can be written as:

$$\hat{H} = \hat{T} + \hat{V}_{ee} + \hat{V}_{ext}, \tag{3.1}$$

where T is the kinetic energy, given by :

$$\hat{T} = -\sum_{i=1}^{N} \frac{1}{2} \nabla_i^2, \tag{3.2}$$

and $\hat{V}_{ee}$ is the electron-electron interaction:

$$\hat{V}_{ee} = \sum_{i=1}^{N} \sum_{j>i}^{N} \frac{1}{r_{ij}}, \tag{3.3}$$

The external field is:

$$\hat{V}_{ext} = \int v(\boldsymbol{r}) \rho(\boldsymbol{r}) \, d\boldsymbol{r} \tag{3.4}$$

For a system with N electrons, if we neglect the spin, this is a set of equations with $3N$ degrees of freedom. It can be imagined that except for some 'toy' systems, a strict solution of the Schrödinger equation in that form is impossible.

Hohenberg and Kohn proved two important theorems which are the cornerstones of DFT [27]. The first Hohenberg and Kohn theorem proves that for a multi-electron system, the electron density distribution function $\rho(\boldsymbol{r})$ is determined uniquely by the external potential. What is more, the Hamiltonian of this system will also be defined by the external potential. Consequently, we can then conclude that the ground state of this system can be expressed as a unique functional of the electron density distribution function $\rho(\boldsymbol{r})$.

The proof of this theorem is not difficult. First, assume that there are two different external fields $\hat{V}_{ext}$ and $\hat{V}'_{ext}$ which correspond to the same density $\rho(\boldsymbol{r})$. Then the Hamiltonians of these two external fields are $\hat{H} = \hat{T} + \hat{V}_{ee} + \hat{V}_{ext}$ and $\hat{H}' = \hat{T} + \hat{V}_{ee} + \hat{V}'_{ext}$, with corresponding wave functions Ψ and Ψ'. The density $\rho(\boldsymbol{r})$ can be then defined as:

$$\rho(r) = N \int \cdots \int \Psi(\boldsymbol{r_1}, \boldsymbol{r_2}, \cdots, \boldsymbol{r_N}) \Psi^*(\boldsymbol{r_1}, \boldsymbol{r_2}, \cdots, \boldsymbol{r_N}) d\boldsymbol{r}_1 d\boldsymbol{r}_2 \cdots d\boldsymbol{r}_N \tag{3.5}$$

According to the variational principle:

$$\begin{aligned} E_0 < \langle \Psi'_0 | \hat{H} | \Psi'_0 \rangle &= \langle \Psi'_0 | \hat{H}' | \Psi'_0 \rangle + \langle \Psi'_0 | \hat{H} - \hat{H}' | \Psi'_0 \rangle \\ &= E'_0 + \langle \Psi'_0 | \hat{V}_{ext} - \hat{V}'_{ext} | \Psi'_0 \rangle \end{aligned} \tag{3.6}$$

Substituting the operator of external field with the integration in Equation 3.4, leading to:

$$E_0 < E'_0 + \int \rho(\boldsymbol{r}) (\hat{V}_{ext} - \hat{V}'_{ext}) d\boldsymbol{r} \tag{3.7}$$

and similarly for $\hat{H}'$:

$$E_0' < E_0 - \int \rho(\boldsymbol{r})(\hat{V}_{ext} - \hat{V}_{ext}')d\boldsymbol{r} \tag{3.8}$$

Adding Equation 3.7 to Equation 3.8 gives:

$$E_0' + E_0 < E_0 + E_0' \tag{3.9}$$

which is a contradiction. The first Hohenberg-Kohn theorem tells us that $\rho(\boldsymbol{r})$ is determined uniquely by the given system. However, we still to find a way to give the real density $\rho(\boldsymbol{r})$.

The second Hohenberg-Kohn theorem tells us how to choose the right $\rho(\boldsymbol{r})$. Briefly [28], this theorem says that if $\rho(\boldsymbol{r})$ is the real density, then the system energy of this $\rho(\boldsymbol{r})$ is the minimum.

Assuming that there are two density distribution function $\rho(\boldsymbol{r})$ and $\rho'(\boldsymbol{r})$which expressed with Equation 3.5. $\rho(\boldsymbol{r})$ is the real density, while $\rho'(\boldsymbol{r})$ is a different distribution. With the lowest energy principle, it can be written that:

$$\begin{aligned} E[\rho'(r)] &= \langle \Psi' | \hat{T} + \hat{V}_{ee} | \Psi' \rangle + \int v(r)\rho'(r)\, dr \\ &> \langle \Psi | \hat{T} + \hat{V}_{ee} | \Psi \rangle + \int v(r)\rho(r)\, dr = E[\rho(r)] \end{aligned} \tag{3.10}$$

These two theorems are the basis of DFT and show that the properties of a solid with N electrons can now be described with the density distribution $\rho(\boldsymbol{r})$ of these electrons. Therefore, the ground state energy of this multi-electron system is a functional of the density. The total energy can be divided into two parts:

$$E_G[\rho] = E[\rho] + V_{ext}, \tag{3.11}$$

where V_{ext} is the external potential which include the nuclei potential. From the previous discussion, the external part V_{ext} is fixed once the external field has been given. The $E[\rho]$ is the functional of density:

$$E[\rho] = T + E_H[\rho(r)] + E_{XC}[\rho(r)] \tag{3.12}$$

where E_H is the Hartree energy which contains a so-called 'self-interaction':

$$\frac{1}{2}\int\int \frac{\rho(r)\rho(r')}{|r-r'|}drdr' \tag{3.13}$$

The E_{XC} is the exchange-correlation energy and T is the kinetic energy. The energy of the electrons in a system is described with equations 3.11—3.13. However, the form of the functionals of kinetic energy and exchange-correlation energy are still unknown.

3.2 Kohn-Sham equations

Hohenberg and Kohn proved that the electron density can be used to solve the multi-electron problem which significantly simplified the process of solving the Schrödinger equation with $3N$ coordinates. One year after Hohenberg and Kohn published their paper, Kohn and Sham provided a practical way to solve the problem of the Hohenberg-Kohn energy functional [5].

In order to find the kinetic energy term and exchange-correlation energy term in Hohenberg-Kohn energy functional, Kohn and Sham first supposed that there

is a fictitious non-interacting system which serves as a reference system. This system has an identical density distribution to the real system. Consequently, the kinetic energy in this reference system can be expressed as the sums of the kinetic energies of single non-interacting electrons while other terms in Hohenberg-Kohn energy functional are expressed as an effective potential. By using this assumption, we can straightforwardly write the Hamiltonian of this system :

$$\hat{H}_{ref} = -\sum_{i}^{N} \frac{1}{2}\nabla_i^2 + \sum_{i}^{N} \hat{V}_{eff}(r_i) \tag{3.14}$$

Therefore, this reference system can be constructed with a series of single particle wave functions:

$$\hat{H}_{ref}\Psi_i(\boldsymbol{r}) = \epsilon_i \Psi_i(\boldsymbol{r}) \tag{3.15}$$

with the requirement on the density that it should be same as the real system.

$$\rho_{ref}(r) = \sum_{i}^{N} \Psi_i(\boldsymbol{r})\Psi_i^*(\boldsymbol{r}) = \rho_G(\boldsymbol{r}) \tag{3.16}$$

It should be noticed that the effective potential $\hat{V}_{eff}(r_i)$ here contains all the complexity of the real system. With this effective potential, we are mapping the problem of the real system onto a single particle problem which is relatively easy. To find out this effective potential, we need to go back to the Hohenberg-Kohn energy functional:

$$
\begin{aligned}
E[\rho] &= T + E_{XC}[\rho] + E_H[\rho] + \int v(r)\rho(r)\,dr \\
&= T_{ref} + (T - T_{ref}) + E_{XC}[\rho] + E_H[\rho] + \int v(r)\rho(r)\,dr \\
&= T_{ref} + \hat{V}_{eff}
\end{aligned}
\tag{3.17}
$$

Here $E[\rho]$ represents the total energy of the ground state and expands the external potential in Equation 3.11 with Equation 3.4.Then the effective potential can be defined as:

$$
V_{eff} = (T - T_{ref}) + E_{XC}[\rho] + E_H[\rho] + \int v(r)\rho(r)\,dr \tag{3.18}
$$

Using the variational method, we can write the Kohn-Sham operator:

$$
\hat{h}_{KS} = -\frac{1}{2}\nabla^2 + \frac{\delta E_H[\rho(r)]}{\delta\rho(r)} + \frac{\delta E_{KS}[\rho(r)]}{\delta\rho(r)} + v(r), \tag{3.19}
$$

where $E_{KS-XC}[\rho(r)]$ is:

$$
E_{KS-XC}[\rho(r)] = E_{XC}[\rho(r)] + (T - T_{ref}), \tag{3.20}
$$

Therefore, if we can find the exact expression for $E_{KS-XC}[\rho(r)]$, we can theoretically calculate the Kohn-Sham equation:

$$
\hat{h}_{KS}\Psi_i = \epsilon_i\Psi_i, \tag{3.21}
$$

where Ψ_i and ϵ_i are usually called the Kohn-Sham orbitals and the Kohn-Sham eigenenergies. But the physical meaning of these orbitals is not clear. In principle, the Kohn-Sham equations would only guarantee that the ground state density and the ground state energy are accurate but cannot ensure that the energy of those orbitals is exactly equal to their ionization energies. Thus, it cannot gives the right band energies for a solid in principle.

The solution of Kohn-Sham equations is self consistent. Starting from a single-particle like reference system which provides an initial density ρ_0, the Kohn-Sham effective potential can be calculated. With this potential, the Kohn-Sham equations can be solved which subsequently gives a new density. This new density is put back into the first step instead of ρ_0. This procedure can be repeated until a self-consistent solution is achieved. This will be discussed further in Section 3.3 and 3.4.

3.3 Exchange correlation functionals

The only remaining problem of solving the Kohn-Sham equations is that we still don't know the exact exchange-correlation interactions E_{XC}. Within the Kohn-Sham framework, E_{XC} is not just about the non-classical exchange-correlation interaction and self-interaction, but also contains the difference in electron kinetic energy between the real and reference systems. In some sense, finding a good quality exchange-correlation expression is one of the most important studies in this area. Unfortunately, it is challenging to find a universally accurate exchange-correlation functional. Consequently, some good substitutes for the real (unknown) exchange-correlation functional have been developed. These substitutes are based on some simple system but still provide an excellent result in many cases.

3.3.1 Local density approximation

One of the simplest multi-electron systems is the homogeneous electron gas (HEG). Starting with this model, Kohn and Sham proved that if $\rho(r)$ is sufficiently slowly varying, the exchange-correlation energy can be seen as only a functional of the local value of the density. This is known as the local density approximation (LDA):

$$E_{XC}^{LDA}[\rho(r)] = \int \rho(r)\varepsilon_{XC}^{HEG}(\rho(r))|_r \, dr, \tag{3.22}$$

where $\varepsilon_{XC}^{HEG}(\rho(r))$ is not a functional of $\rho(\boldsymbol{r})$ but the exchange-energy of the HEG at position $\boldsymbol{r}$. It can be divided to two parts:

$$\varepsilon_{XC}^{HEG}(\rho(r)) = \varepsilon_{X}^{HEG}(\rho(r)) + \varepsilon_{C}^{HEG}(\rho(r)) \tag{3.23}$$

In general, ε_X can be written as [29]:

$$\varepsilon_X = -\frac{3}{4}\left(\frac{3\rho(r)}{\pi}\right)^{1/3} \tag{3.24}$$

As for the correlation part of the HEG, an explicit form of the energy functional is difficult to calculate theoretically, but there are many quantum Monte-Carlo simulations of the correlation energy which have been proved to be accurate [30,31].

Neglecting the error of the quantum Monte-Carlo simulation, LDA can be seen as a very accurate description of the exchange-correlation energy of the HEG. Since the real system is likely to be far away from the HEG system, at first sight, a DFT-LDA calculation might not be expected to give a good result. However, many calculations have indicated that the LDA shows a good agreement with experiments, especially for *s*- and *p*-electron solids. In conclusion, the LDA is a

good starting point and gives an acceptable result for some solid crystals which have a relatively uniform electron density distribution [5]. As for molecular systems or d- and f-electron solids, it could possibly give wrong results [7].

3.3.2 Generalized gradient approximation

The model of LDA is extracted from HEG which assumes that the exchange-correlation interaction is just a functional of the density at some particular point r. This approximation requires that $\rho(r)$ varies very slowly. When the density is not uniform anymore, the variation of $\rho(r)$ should be added to correct this heterogeneity. The gradient of the density has been considered as a correction for the inhomogeneous electron density. It is known as the generalized gradient approximation (GGA) [7]:

$$E_{XC}^{GGA}[\rho(r)] = \int f(\rho(r), \nabla\rho(r))\, dr, \tag{3.25}$$

The specific form of the function f is usually given by some empirical parameters. Therefore, some GGA functionals may be established from experimental fitting. GGA also shows a good performance on material predictions. A classic example is the incorrect ground state of Fe that is predicted by LDA to be nonmagnetic and face-centred cubic, but which is corrected by GGA [32]. Another great improvement of GGA is about the ionization energies of materials. For the molecule systems for which the LDA tend to underbind, like H_2 or CH_4, GGA shows a very good agreement with experiments [33].

3.4 DFT in practice

Based on Kohn and Sham's work, all the DFT calculation can be solved self-consistently with the flow chart shown in Figure 2.

The interactions between the nuclei and the electrons are Coulombic. So there will exist a singularity in the Coulomb potential when $r \to 0$. For those electrons close to the centre of nuclei, the potential varies very fast while those outer electrons may feel a smooth potential. Therefore, a simple idea to handle the potential problem is to treat them as two parts, a core part and an interstitial part. This is the so-called 'muffin-tin'(MT) approximation [34, 35].

Combined with the MT shape approximation, the full potential(FP) of an atom in a solid can be expressed as two parts. The core states were treated as a sphere with spherical symmetry which can be described by radial functions. As for the outside region, the potential is supposed to be a constant. The continuity condition requires that the wavefunction is continuous at the boundary of two regions. Different from the pesudopotential method [16], both the valence electrons and core electrons are considered in this FP method.

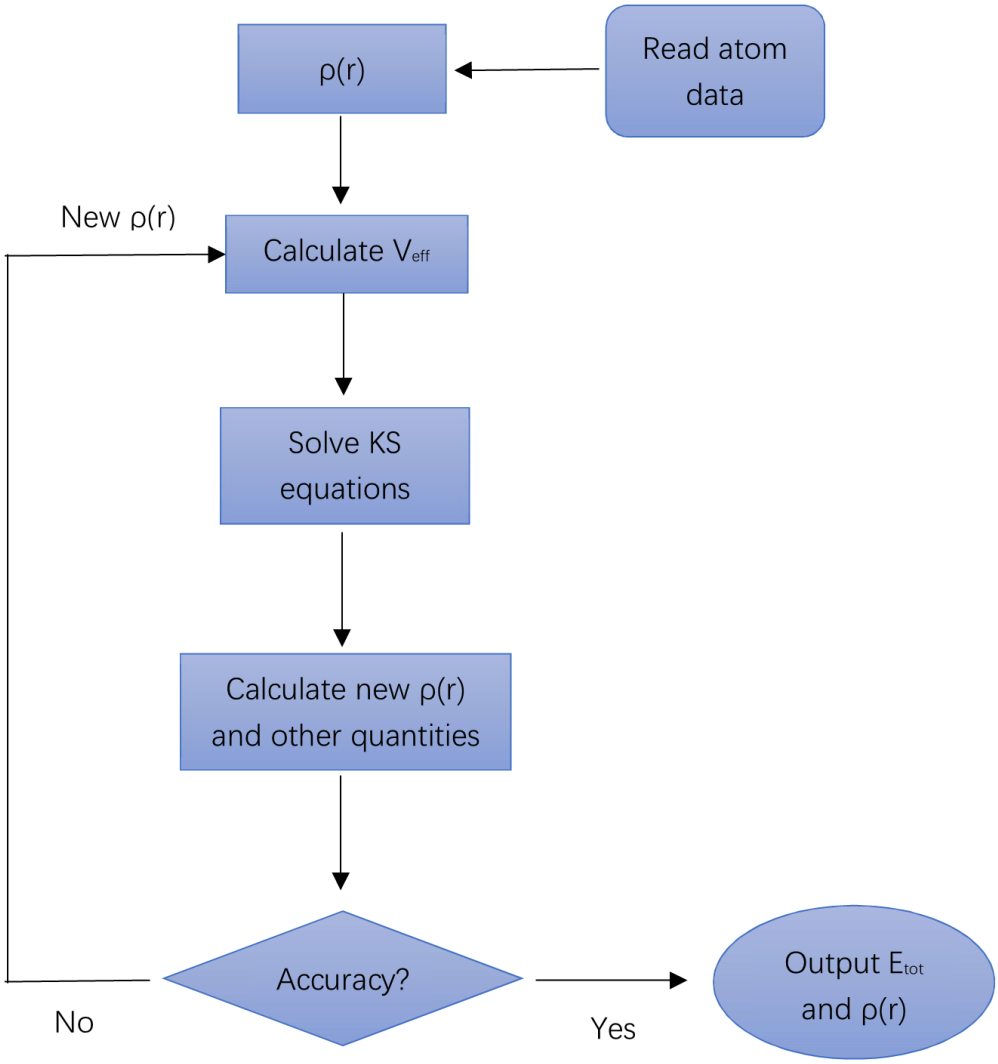

Figure 2: Schematic diagram of DFT calculation.

3.4.1 Augmented planewave method

According to the MT model, for an atom α, the basis can be divided into two regions:

$$\phi(\boldsymbol{r}) = \begin{cases} \frac{1}{\sqrt{\Omega}} \sum_G c_G e^{i(\boldsymbol{G}+\boldsymbol{k})\cdot \boldsymbol{r}}, & r \in interstitial \\ \sum_{lm} A^{\alpha}_{lm} u^{\alpha}_{l}(\boldsymbol{r}, E) Y_{lm}(\boldsymbol{r}), & r \in sphere \end{cases} \tag{3.26}$$

where Ω is the volume of unit cell, A_{lm} and c_G are the expansion coefficients. The region $r \in interstitial$ is the outer part of the MT model which the wavefunctions are expanded in plane waves, while the region $r \in sphere$ is the inner core part which uses an expansion in spherical harmonic functions. $u_l(r)$ are the radial solutions of the Schrödinger equation at the desired energy:

$$[-\frac{d^2}{dr^2} + \frac{l(l+1)}{r^2} + V(r) - E_l]ru_l^{\alpha}(r, E) = 0 \tag{3.27}$$

In order to satisfy the continuity conditions, it is required that the value of the wavefunction inside the spherical part should be equal to that outside the sphere. This matching coefficient A can be found by requiring that the spherical harmonic basis functions match the plane waves in the interstitial region at the boundary. However, the problems have not all been solved. The energy E_l in Equation 3.27 has not been determined yet. This energy is exactly what we want to know and which should be the eigenenergy of a state. In another word, the radial function $u_l(r)$ is not energy independent which will lead to a non-linear secular equation. In practice, a trial energy must be chosen beforehand, and it will be solved self-consistently until we find the right energy for this state. This procedure will be repeated for all the states. It is clear that the computational resource requirements for the augmented planewave method(APW) method will be relatively large. Another problem of the APW method is that if at some point inside the sphere, the radial function $u(r)$ is zero, then we cannot find an appropriate coefficient, especially for electrons in d or f bands. This is known as the asymptote problem [36].

3.4.2 Linearized augmented plane wave method

The biggest problem for APW is that the radial functions inside the spheres are energy dependent which means that for each eigenvalue the APW's must be solved

self-consistently to find the right eigenenergy. To solve this problem, we expand the $u_l(r)$ in a Taylor series:

$$\begin{aligned} u_l(r,E) =& u_l(r,E_l^0) + (E-E_l^0)\frac{\partial u_l(r,E)}{\partial E}|_{\,E=E_l^0} + \frac{(E-E_l^0)^2}{2}\frac{\partial^2 u_l(r,E)}{\partial E^2}|_{\,E=E_l^0} \\ &+ O(E-E_l^0)^3 + \cdots \end{aligned} \tag{3.28}$$

The first term of the series expansion is same as the u in APW and the second term can be solved by:

$$\left[-\frac{d^2}{dr^2} + \frac{l(l+1)}{r^2} + V(r) - E_l\right] r\dot{u}_l^\alpha(r,E) = r u_l^\alpha(r,E) \tag{3.29}$$

Then, the new basis is:

$$\phi(\boldsymbol{r}) = \begin{cases} \frac{1}{\sqrt{\Omega}}\sum_G c_G e^{i(\boldsymbol{G}+\boldsymbol{k})\cdot\boldsymbol{r}}, & r \in interstitial \\ \sum_{lm}[A_{lm}^\alpha u_l^\alpha(\boldsymbol{r},E) + B_{lm}^\alpha \dot{u}_l^\alpha(\boldsymbol{r},E)]Y_{lm}(\boldsymbol{r}), & r \in sphere \end{cases} \tag{3.30}$$

The interstitial region is still described by plane waves while a new term with the derivative of u has been introduced into the basis in the MT sphere. Consequently, a new group of coefficients A and B are required for matching both the value and slope at the boundary of the sphere. This is the Linearized Augmented Plane Waves method(LAPW) [37]. Although LAPW adds some new matching conditions, the secular equation can be solved with a single diagonalization procedure because the $u_l(r)$ are not energy dependent but l dependent. Therefore, the big improvement of LAPW is that the computational cost decreases significantly by introducing a new variational variable.

3.4.3 Augmented plane waves plus local orbitals

However, for some low-lying states which have the same quantum number l as valence states but different n, a good energy E is difficult to find. For solving these 'semi-core' states, another basis was added which are the so called Local orbitals(LO) [38]:

$$\phi(\boldsymbol{r}^{lo}) = \begin{cases} 0, & r \in Interstitial \\ \sum_{lm}[A^{lo}_{lm,\alpha} u^{\alpha}_{l}(\boldsymbol{r}, E) + B^{lo}_{lm,\alpha} \dot{u}^{\alpha}_{l}(\boldsymbol{r}, E)]Y_{lm}(\boldsymbol{r}), & r \in Sphere \end{cases} \tag{3.31}$$

It should be noticed that the derivative of u_l was also in the basis of LO. In contrast to the LAPW method, the matching conditions of LO require that both the value and gradient should be zero at the boundary of the MT sphere. Therefore, the energy dependent problem was solved by introducing new LO and the size of the basis is approximately the same as the APW method.

3.4.4 The limitations of DFT

Since Kohn and Sham published their paper about the solution of the energy functionals, thousands of great researchers have been working in this area over several decades. But sometimes DFT does not predict or describe the experimental data very well. This is mainly because we cannot find the exact form of the energy functional that is described in HK theorem. The most famous problem with DFT is the wrong prediction of the band gap. It is usually systematically underestimating the band gap in semiconductors. It is worse in d/f elements and may even predict an insulator as a conductor. What is more, the excited-states prediction of material is also beyond the ability of DFT. There is no theory to ensure that DFT calculations will give exact orbitals of systems. This is partly

due to the poor approximation of exchange-correlation functionals. However, if we find an exact exchange-correlation functional which means that the KS-DFT theory has no approximations, we still cannot say that we can calculate everything about a solid. This is because, in principle, the HK theorem only requires that the ground state energy and density are equal to those in a real system [14].

In addition, the power of computers also restricts us. In solid state physics, a candidate system may consist of a unit cell with tens of atoms with a periodical structure. However, for those big molecules with hundreds or thousands of atoms, an accurate calculation may spend weeks or months. But for a drop of water, it contains trillions of atoms, a calculation is far beyond our ability.

4 The GW method

The standard DFT theory provides us a way to calculate the properties of solids by solving the KS equations. However, DFT is not a perfect tool that is able to give all information of materials. As discussed before, the gap problem corresponding to the photoemission experiments indicates that the DFT is a ground state theory and it becomes invalid when calculating the excited properties. Furthermore, an accurate DFT calculation is based on the quality of exchange-correlation functionals. For the strongly-correlated materials which often have d and f band electrons, DFT calculations may lead to a wrong result as well. Several methods have been developed to solve the complex correlated problems such as hybrid functionals, LDA+U and dynamic mean-field theory [39]. One of the most accurate methods of studying the spectral properties and correlated problems is the GW approximation (GW). GW is based on Hedin equations which is designed to describe the behaviours of quasi-particles. The GW can be seen as an extension of the Hartree-Fock approximation by replacing the bare Coulomb potential with the dynamically screened potential W [13, 40]. By solving Hedin's equations, the Green's function which is the solution of Hedin equations contains the information about the density distribution and the eigenenergies of the studied system. Thus, the band structure and the Fermi surface can be then reconstructed from the Green's function in k space. Although the GW method was presented in the 1960s [13], practical calculations were restricted by computer science. It was in 1980 that Hybertsen and Louie first calculated a group of semiconductors with the GW and showed a good result [41]. After that, much research has shown that GW is one of the best theoretical ways to correct the gap problem and the strongly-correlated problem of materials. In this chapter, we will shortly discuss the theoretical background of the GW method and present some calculations as examples of the GW to show its performance. All the calculations are based on

Elk code.

4.1 Theory of the GW method

4.1.1 Single-particle Green's function

As mentioned above, the GW method is a Green's function method. The single-particle Green's function is defined as [42]:

$$iG(t-t^{'},\boldsymbol{k}) = \left\langle N|T[\hat{\psi}_{\boldsymbol{k}}(t)\hat{\psi}^{\dagger}_{\boldsymbol{k}}(t^{'})]|N\right\rangle, \tag{4.1}$$

where N is the N particle ground-state, ψ and $\psi^{\dagger}$ are the field operator under the Heisenberg representation and T is the time-ordering operator. Thus, the single-particle Green's function can be rewritten with a single equation:

$$G = G^{e} - G^{h}, \tag{4.2}$$

where G^{e} and G^{h} are the Green's function (propagator) of an electron and a hole, respectively:

$$\begin{aligned} iG^{e}(t-t^{'},\boldsymbol{k}) &= \left\langle N|\hat{\psi}_{\boldsymbol{k}}(t)\hat{\psi}^{\dagger}_{\boldsymbol{k}}(t^{'})|N\right\rangle \theta(t-t^{'}) \\ iG^{h}(t-t^{'},\boldsymbol{k}) &= -\left\langle N|\hat{\psi}^{\dagger}_{\boldsymbol{k}}(t^{'})\hat{\psi}_{\boldsymbol{k}}(t)|N\right\rangle \theta(t^{'}-t), \end{aligned} \tag{4.3}$$

where θ is the Heaviside step-function. Noticing that the time dependence of operator is :

$$\hat{\psi}_{\boldsymbol{k}}(t) = e^{iHt}\hat{\psi}_{\boldsymbol{k}}e^{-iHt} \tag{4.4}$$

The Green's function can be expressed as [42]:

$$iG(\boldsymbol{k},\tau) = \theta(\tau)e^{-i\tau\varepsilon} - \theta(-\tau)e^{-i\tau\varepsilon} \tag{4.5}$$

where $\tau = t - t^{'}$. In order to study the Green's function in frequency space, Fourier transformation was applied to the Equation 4.5. The Fourier transformation of the step function is:

$$\Theta(\omega) = \frac{1}{2\pi}\int_{-\infty}^{\infty}\theta(\tau)e^{i\omega\tau-\eta|\tau|}, d\tau = \frac{i}{2\pi(\omega+i\eta)} \tag{4.6}$$

Thus, the Green's function in frequency space has the following form:

$$G(\boldsymbol{k},\omega) = \sum_{n}\frac{\psi_n(k)\psi_n^*(k)}{\omega - \varepsilon_n(\boldsymbol{k}) \pm i\eta}, \tag{4.7}$$

where n is the index of the state and ψ is the wavefunction. The physical meaning of the pole of Green's function is clear from Equation 4.7. The poles correspond to the eigenenergy of the system. The density of states can be also derived from Green's function through:

$$\rho(\omega) = \sum_{n}\psi_n(k)\psi_n^*(k)\delta(\omega - \varepsilon_n) \tag{4.8}$$

With the identity:

$$\lim_{\eta\to 0}\frac{1}{x \pm i\eta} = P\frac{1}{x} \mp i\pi\delta(x) \tag{4.9}$$

where P is the principal value. Equation 4.7 can be written as:

$$G(\boldsymbol{k},\omega) = P\sum_{n}\frac{\psi_n(k)\psi_n^*(k)}{\omega-\varepsilon_n(\boldsymbol{k})} \mp \sum_{n} i\pi\delta(\omega-\varepsilon_n)\psi_n(k)\psi_n^*(k) \tag{4.10}$$

Therefore, the density of states ρ can be expressed with the imaginary part of Green's function:

$$\rho(\omega) = \frac{1}{\pi} Im[G(\omega)] \tag{4.11}$$

This is usually called the spctral function:

$$A(\boldsymbol{k},\omega) = \frac{1}{\pi} Im[G(\boldsymbol{k},\omega)] \tag{4.12}$$

The Green's function can be also expressed with the spectral function:

$$G(\boldsymbol{k},\omega) = \int_{\infty}^{\infty} \frac{A(\boldsymbol{k},\omega^{'})}{\omega-\omega^{'}\pm i\eta}, d\omega^{'} \tag{4.13}$$

Theoretically, the single-particle Green's function contains all the information about the Hamiltonian. From Equation 4.11 4.12, the spectral function of a particular k point is in fact the local density of states of that point. In real solids, the complex interaction between electrons is described with the self-energy which will be discussed in next section.

4.1.2 Dyson equation and the self-energy

For a real system, the interaction between electrons is governed by the self-energy $\Sigma(r,r^{'};\omega)$ [24]. The connection between the Green's function and the self-energy can be expressed via the Dyson equation which is established from the perturbation

expansion of the Green's function [23, 43]:

$$G = G^0 + G^0 \Sigma G, \tag{4.14}$$

where G^0 is the non-interacting single-particle Green's function that neglects the exchange and correlation effects beyond the Hartree approximation [43] and G is the Green's function that corresponds to the interacting system. It is usually rewritten with a simpler form:

$$G^{-1} = (G^0)^{-1} - \Sigma, \tag{4.15}$$

The Dyson equation provides a way to calculate the interacting Green's function G by finding the self-energy Σ. With the concept of self-energy, we can write the equation for the quasi-particles [13, 14]:

$$[-\frac{1}{2}\nabla^2 + V_H(r) + V_{ext}]\psi_i(r) + \int \Sigma(r, r^{'}; \varepsilon_i)\psi_i(r^{'})dr^{'} = \varepsilon_i \psi_i(r), \tag{4.16}$$

where V_H is the Hartree potential, V_{ext} is the external potential and ε_i is the quasi-particle energy. It can be found that the quasi-particle equation has a similar form to the KS Equation 3.19 and 3.21. In this respect, different single-particle theories like DFT can be seen as a trial of finding an appropriate approximation of the self-energy which contains the complex exchange and correlation interactions [14].

However, pratical task of calculating an accurate self-energy is extremely difficult because it contains all the expanded terms of interacting Green's function. Fortunately, there are some effective approximations which can be used to obtain a good description of the self-energy; one such approximation is the GW [40].

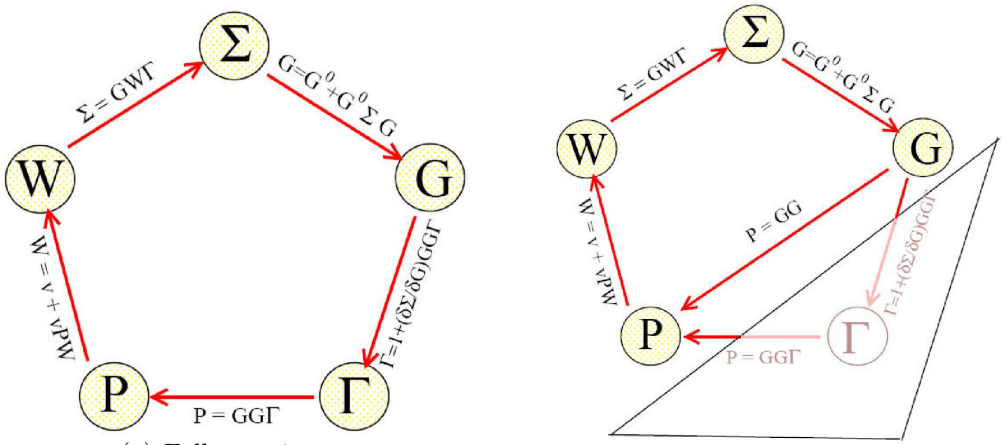

(a) Full equations (b) GW approximation

Figure 3: Full Hedin equations shown in (a), GW approximation shown in (b) [1].

4.1.3 Hedin equations

It was Hedin who summarized a group of coupled integral equations to solve the self-energy problem [13]:

$$\begin{aligned}
\Sigma(1,2) &= i\int G(1,4)W(1^+,3)\Gamma(4,2;3)d(3,4),\\
W(1,2) &= v(1,2)+\int W(1,3)P(3,4)v(4,2)d(3,4),\\
P(1,2) &= i\int G(2,3)G(4,2)\Gamma(3,4;1)d(3,4),\\
\Gamma(1,2;3) &= \delta(1,2)(1,3)\\
&\quad+\int \frac{\delta\Sigma(1,2)}{\delta G(4,5)}G(4,6)G(7,5)\Gamma(6,7;3)d(4,5,6,7)
\end{aligned} \tag{4.17}$$

The natural number in the equations is a group of space-time coordinates: $1 = (\boldsymbol{r}_1, t_1)$ and $1^+ = (\boldsymbol{r}_1, t_1+\eta)$. P is the irreducible polarizability, W is the dynamically screened potential, v is the bare Coulomb potential, Γ is the vertex function. It is clear that the Hedin equations can be solved self-consistently. But the most

difficult part of solving these equations is the functional derivative part in the expression for the vertex function Γ. Therefore, an approximation was applied to simplify the vertex function that neglects the integration part of Γ. By taking $\Gamma = \delta(1,2)\delta(1,3)$, the GW consequently allows the self-energy to be expressed in a simpler form:

$$\Sigma \approx iGW \tag{4.18}$$

As shown in Figure 3, the Hedin equations can be now rewritten as:

$$\begin{aligned} \Sigma(1,2) &= iG(1,2)W(1^+,2), \\ W(1,2) &= v(1,2) + \int W(1,3)P(3,4)v(4,2)d(3,4), \\ P(1,2) &= -iG(1,2)G(2,1). \end{aligned} \tag{4.19}$$

The Green's function can be obtained by solving these equations self-consistently. In practical, the non-interacting Green's function G^0 is usually from the DFT calculation which contains some exchange-correlation interactions V^{XC}. Consequently, the self-energy and the Hedin's equations become [14]:

$$\Delta\Sigma = \Sigma - V^{XC}_{DFT}, \tag{4.20}$$

$$G = G^0 + G^0\Delta\Sigma G \tag{4.21}$$

4.1.4 Dynamically screened interaction

The self-energy is written as the product of the Green's function G and the dynamically screened potential W via Equation 4.18. In practice, the inverse dielectric function ϵ^{-1} is at the core of solving the screened potential W [14]:

$$\begin{aligned}\epsilon^{-1} &= \frac{\delta V}{\delta \phi} \\ &= 1 + v\frac{\delta \rho}{\delta \phi} \\ &= 1 + v\frac{\delta \rho}{\delta V}\frac{\delta V}{\delta \phi},\end{aligned} \tag{4.22}$$

where ρ is the charge density, ϕ is the external field, V is the total field. The response function R and the polarization function P are defined as:

$$R = \frac{\delta \rho}{\delta \phi}, \tag{4.23}$$

and

$$P = \frac{\delta \rho}{\delta V}, \tag{4.24}$$

Thus the inverse dielectric function can be expressed with the response function or the polarization function:

$$\begin{aligned}\epsilon^{-1} &= [1 - vP]^{-1} \\ &= 1 + vR\end{aligned} \tag{4.25}$$

Together with the expression of W in Equation 4.19, we have [14, 44]:

$$\begin{aligned}W &= v + vPW \\ &= v + vRv \\ &= \epsilon^{-1}v\end{aligned} \tag{4.26}$$

4.1.5 GW method in practice

With the GW approximation neglecting the vertex function, the solution of the Hedin equations is also self-consistent which means that the results do not depend on the initial state. However, the full self-consistent GW calculation is very expensive due to the difficulties of calculating the inverse dielectric function ϵ^{-1}. Therefore, a widely used method is the single-shot GW calculation, G^0W^0. In a G^0W^0 calculation, the interacting Green's function would be calculated only once. Consequently, without a self-consistent calculation loop, the starting point of G^0W^0 will significantly influence the results. From previous work, it has been shown that it is fortunate that the orbitals from Hartree-Fock approximation(HFA), LDA and GW are very close [45]. Thus, it is reasonable to use the results from DFT-LDA as the starting point for G^0W^0 calculation. What is more, the self-energy calculation is usually performed in the imaginary time domain in practice [46]. Consequently, the N-point-Padé analytic continuation procedure is applied to calculate the self-energy on the real energy axis [1, 47]. However, it is worthy to note that this porcedure will usually introduce some numerical noise.

The 'non-interacting' Green's function G^0 is built from the KS-LDA eigenenergy ε with Equation 4.7:

$$G^0_{LDA}(\omega) = \frac{1}{\omega - \varepsilon_{LDA} + i\eta} \tag{4.27}$$

The dynamically screened potential W can be derived from 4.26 with the inverse dielectric function ϵ^{-1}. The dielectric function is usually calculated with the random phase approximation (RPA) [44, 48]; a full description of the RPA is beyond the scope of this dissertation. With the inverse dielectric function, we can

calculate the self-energy with G^0_{KS}:

$$\begin{aligned} W^0 &= \epsilon^{-1}_{RPA} v \\ \Sigma &= iG^0 W^0 \end{aligned} \tag{4.28}$$

Thus, we can write the interacting Green's function G in frequency space:

$$G_i(\omega) = \frac{1}{\omega - \varepsilon_i - \Sigma_i(\omega)} \tag{4.29}$$

In the Elk code, the Green's function is calculated for each irreducible k-point in the BZ (which has its own weight). Thus, the total spectral function in the first BZ is the weighted summation of the spectral functions for each k-point. What is more, with the spectral for each k-point, we can construct the quasi-particle distribution in the first BZ by integrating the spectral function in energy(frequency) space:

$$n(\boldsymbol{k}) = \int_{-\infty}^{E_f} A(\boldsymbol{k}, \omega) d\omega, \tag{4.30}$$

where E_f is the Fermi energy, A is the spectral function as shown in Equation 4.12. The lower limit of the integration is the lowest eigenenergy of the calculation. The Fermi energy is defined via the total spectral function(TSF) A_{tot}:

$$A_{tot}(\omega) = \Sigma_{\boldsymbol{k}} A(\boldsymbol{k}, \omega) \Omega(\boldsymbol{k}), \tag{4.31}$$

where $\Omega(k)$ is the weight function of the k-point. Thus the Fermi energy can be evaluated with the integration of TSF:

$$n_v = \int_{-\infty}^{E_f} A_{tot}(\omega) d\omega, \tag{4.32}$$

where n_v is the number of valence electrons of the studied system. The Fermi

surface can be then contoured from the occupancy of quasi-particles in the first BZ.

4.2 GW calculation for simple systems

For testing the performance of the GW calculations in the Elk code and understanding the physical meaning of the results, a group of well-studied materials was chosen.

4.2.1 Semiconductors and insulators

One of the most important improvements of GW calculation is the correction of the band gap. Three simple materials: LiF, BN(cubic) and C (diamond) were chosen to illustrate the difference between GW and the LDA.

Material	Space group	Lattice constant(Å)
cubic-BN	F-43m	a=b=c=3.6150 [49]
diamond-C	Fd-3m	a=b=c=3.5668 [50]
LiF	Fm-3m	a=b=c=4.0100 [51]

Table 1: Lattice constants of semiconductors and insulators.

As discussed before, the quality of a single-shot GW calculation is sensitive to previously calculated LDA orbitals. From the point of view of the numerical implementation, a good ground-state calculation will not only provide an appropriate starting point but can also significantly reduce the numerical errors that come from the transformation from the imaginary time domain to real energy axis of the spectral functions. Therefore, a high-quality LDA calculation was required before performing the single-shot G^0W^0 calculation. A relatively dense k-space sampling with k-point mesh of $16 \times 16 \times 16$ for all three materials. The number of irreducible k-points for BN, C and LiF were 245, 145 and 145, respectively. The plane-wave cutoff is $R_{MT}|G+K|_{max} = 8.0$ for all materials while the MT radii for

B, N, C, Li and F were1.4540 a.u., 1.4540 a.u.,1.4315 a.u., 1.7782 a.u. and 1.4540 a.u., respectively. The lattice constants and structures are shown in Table 1.

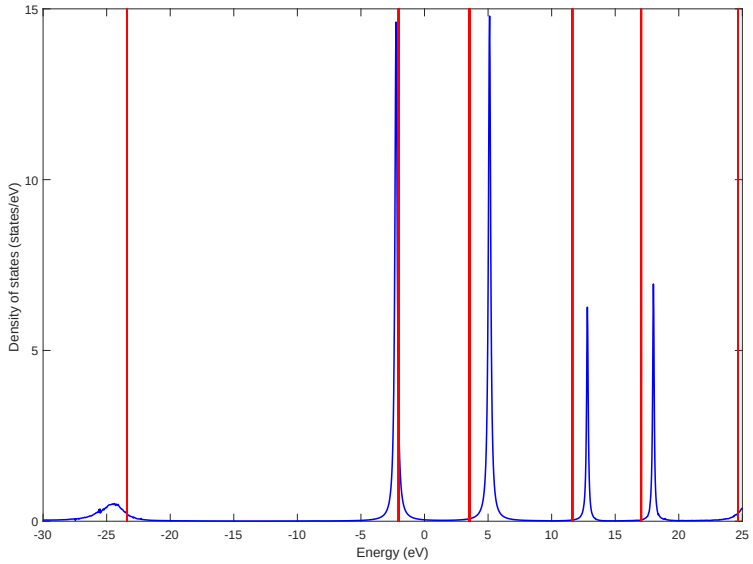

Figure 4: The eigen value and spectral function of diamond at Γ point.The eigen value from DFT calculation is shown in red while spectral function is in blue.

As shown in Figure 1 and 4, a sharp 'state peak' is not expected to be found from the quasi-particles' spectral functions. Comparing with the sharp 'spikes' of eigen value in Figure 4 which represent two degenerate electrons, the peaks of spectral functions of quasi-particles has a obvious width. The excitation of electros which is also the nature of quasi-particles is the main reason of such phenomenon. The width of the peak is the reciprocal of the quasi-particle. The shift of the peaks is the result of the correction of GW method.

The quasi-particle peak will creat a long tail at the band edge. Therefore, as shown in Figure 5, here we choose $n(E) \leq 0.05$ as the band edge to estimate the band gap.

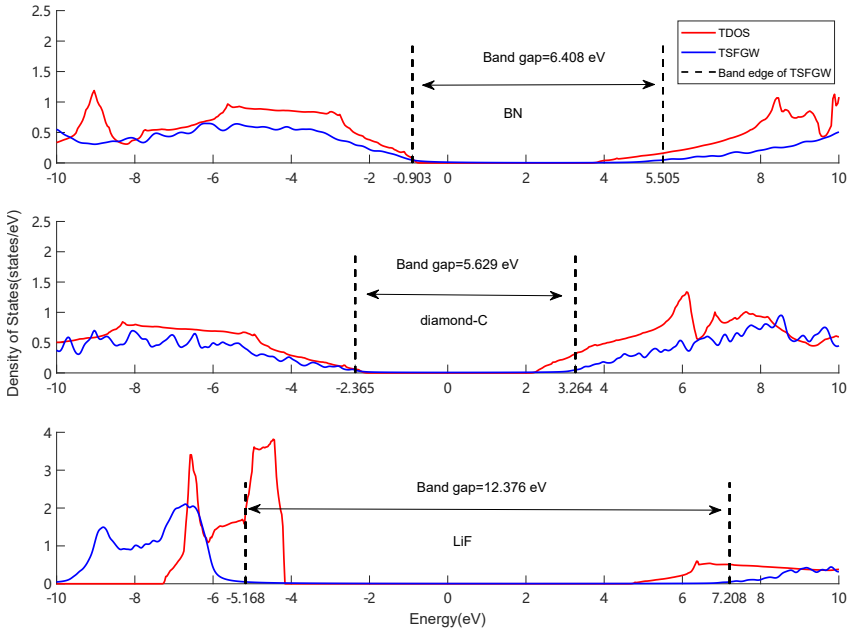

Figure 5: The total density of states(TDOS) and the total spectral function(TSFGW) of insulators and semiconductors.

It is obvious that for each material the spectral function and DOS have similar structure while the band gap of the TDOS is narrower than that from TSF. The results of the single-shot G^0W^0 calculations are in agreement with experiments as shown in table2. Especially for LiF, the LDA calculation underestimates the band gap by around 40% while it is only 10% for the G^0W^0 calculation. From a theoretical point of view, such a big difference is because that DFT-KS equation is aimed at finding the ground-states of solids, while GW method is designed for describing the excited spectra. Although it is a single-shot calculation with only one iteration, a full self-consistent GW calculation may not necessarily provide a better result [52, 53].

What is more, the numerical noise from the analytical continuation procedure is very small here. This is because only very few k-point is significantly inluenced by such noise. So When calculating the total spectral function, the numerical noise will be smeared out by Equation 4.31.

In conclusion, the GW method successfully corrects the gap problem of the LDA. A better prediction of the band gap of semiconductors and insulators is obtained from single-shot G^0W^0 calculation based on Elk code. A series of metals (which of course have Fermi surfaces) will be studied in the next section.

	LDA(eV)	GW(eV)	expt.(eV)
cubic-BN	4.3	6.408	6.3 [54]
diamond-C	4.1	5.629	5.4 [16]
LiF	8.8	12.376	14.4 [55]

Table 2: Estimated band gap of semiconductors and insulators.

4.2.2 Metals

The existence of a Fermi surface is the key characteristic of a metal. Consequently discovering the shape or other properties related to the Fermi surface will help us to understand the singular behaviours of metals such as superconductivity. In Fermi liquid theory, the quasi-particle will also form a Fermi surface with an occupation change for quasi-particles in the first BZ. In this section, the occupancy distribution in the first BZ is obtained from spectral functions. Thus, the Fermi surface can be constructed. For testing purpose, Li and Cu were chosen as a typical simple metal with well defined Fermi surfaces to show the performance of the single-shot G^0W^0 calculation in Elk.

The GW calculation for metals is also based on high-quality LDA results. The k grid in first BZ for Li and Cu are $16 \times 16 \times 16$, leading to 145 irreducible k-points in first BZ for Li and Cu. $R_{MT}|G+K|_{max} = 8.0$ for Li and Cu while the radii of the MTs were 1.8000 a.u. and 2.3902 a.u., respectively. The lattice constant and space group are shown in Table3. The analytic continuation procedures are performed. However, it can be found from Figure 6, the numerical noise from the analytic continuation procedure procedures will lead to a variation of the occupation at

some particular points. For simple metals such as Li, the noise is very samll and won't change the structure of Fermi surface as shown in 8. But for Cu, the noise is relatively strong which lead to a slight distortion of the Fermi surface of Cu.

	space group	lattice constant(Å)
Li	m-3m	a=b=c=4.0495 [56]
Cu	Fm-3m	a=b=c=3.6150 [57]

Table 3: Lattice parameters and structures for Li and Cu.

The spectral function is calculated for each k point, so an integration over the energy of the spectral function for a particular k point can be seen as the quasi-particle occupation for that k point. Using the symmetry operations, the occupation distribution of irreducible k points can be then extended to the first BZ with Equation 4.30. The Fermi surface is contoured from the filled states in the first BZ.

However, different from the DFT eigen value, the number of the quasi-particles of some particular k point is not expected to obtained by counting peaks. This is because the so-called satellite peaks of spectral functions [58]. As shown in Figure 7, the main quasi-particle peak which has a relative higher density of states is accompanied by a series of satellite peaks with slightly lower density of states. What is more, the width of the quasi-particles peaks in spectral functions are around 0.5eV or larger. So it's difficult to define the position of the electron peaks as well. But the integration of all these peaks is equal to the expected number of electrons due to the quasi-particle nature. From the DFT calculation, only four electrons at this point. Therefore, the number of quasi-particles at an particular k points is determined by the integration in Equation 4.30.

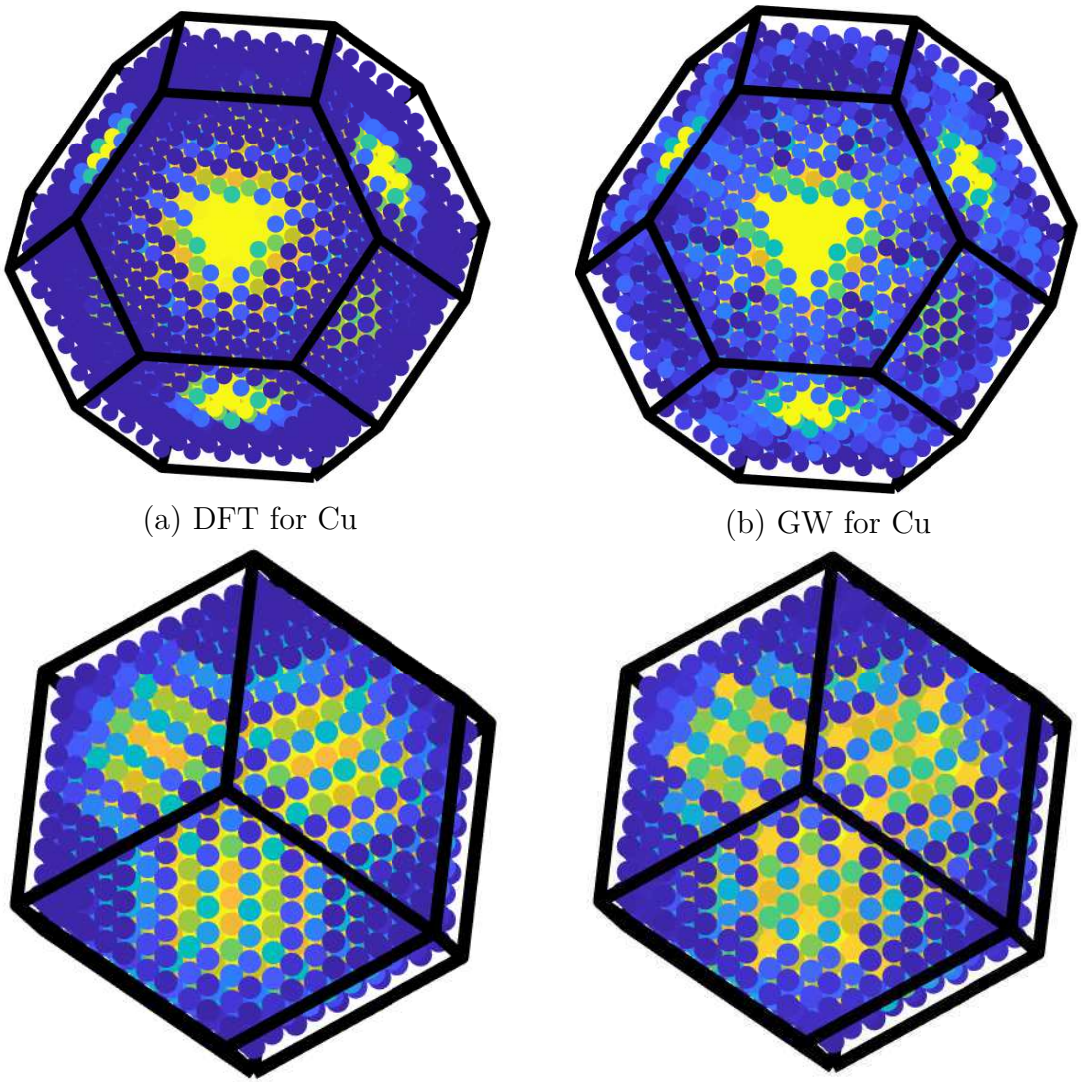

(a) DFT for Cu

(b) GW for Cu

(c) DFT for Li

(d) GW for Li

Figure 6: 3D electron distribution of Li and Cu in FBZ. High occupation k points are shown in yellow while blue for low occupation.

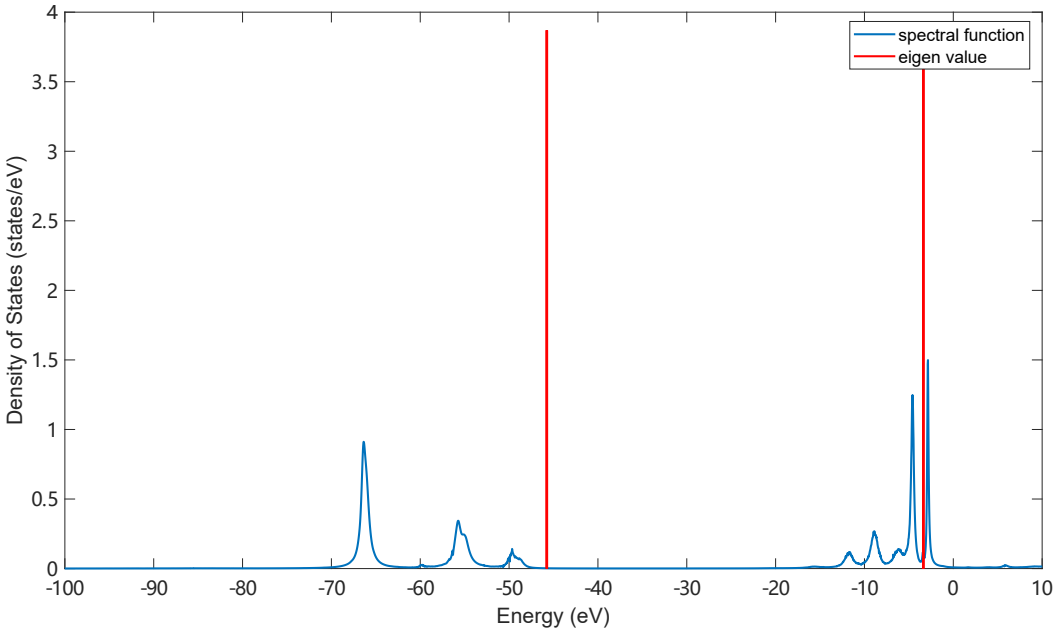

Figure 7: The spectral function of Li at Γ point.

Theoretically, the Fermi surface is where the number of electrons changes. In practice, the Fermi surface is contoured by an isovalue which is usually the middle value between the highest number of electrons and the lowest number of electrons.

For Li with one valence electron, this value is $n(k) = 1.5$. The Fermi surface for Li from both the LDA and GW is shown in Figure 8.

As the simplest metal with only three electrons, the behaviours of valence electrons in Li is very close to that described by the free electron approximation. Thus Li was predicted with a sphere-like Fermi surface [59] as shown in Figure 8.

In contrast to Li, the Fermi surface of Cu is distorted due to the proximity of the Fermi surface to the boundary of the BZ. The existence of necks at the Fermi surface is beyond the predictions of the free electron model [60]. With 17 valence electrons and two degenerate electrons at the highest occupied state, the isovalue for Cu is $n(k) = 17$ The calculated Fermi surface of Cu is shown in Figure 9.

The necks are visible in both GW and LDA. GW and LDA provide the same

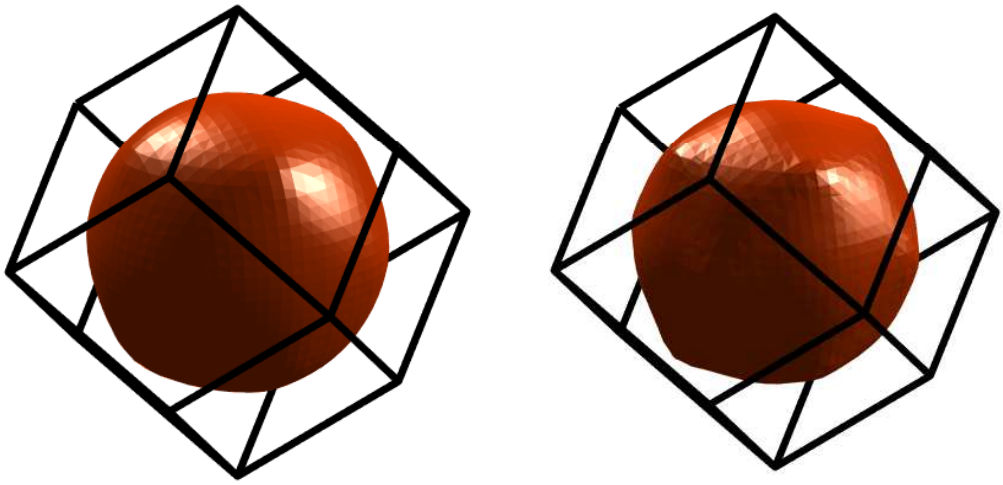

(a) LDA (b) GW

Figure 8: Fermi surface for Li calculated using the LDA (left) and the GW (right).

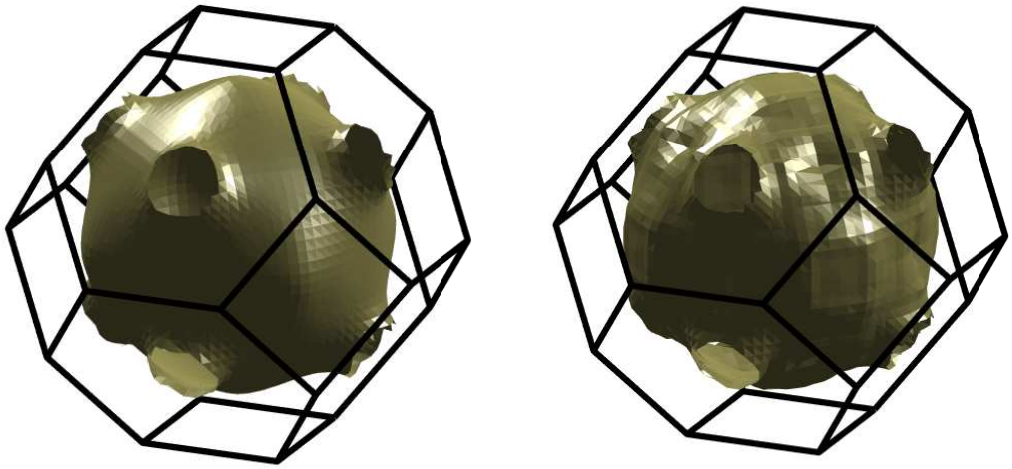

(a) LDA (b) GW

Figure 9: Fermi surface for Cu calculated using the LDA (left) and the GW (right).

result for Cu while the variations seen in the FS from the GW is due to the numerical noise that was discussed at the beginning of this section. It proves that our method of reconstructing the Fermi surface is feasible. By comparing to the experimental Fermi surface, GW calculations can also give detailed information of electron distribution in momentum space.

5 Co_2MnSi

5.1 Introduction

In 1893, a German scientist F. Heusler [10] found a new class of ternary magnetic compounds which consisted of three non-magnetic elements. Today, these compounds are known as the Heusler alloys. Full Heusler alloys have a general chemical formula of X_2YZ, where X and Y are transition metals and Z is from the *p*-block elements. Restricted by the experimental and theoretical conditions at that time, systematic study of this novel material was slow. In 1983, de Groot found that in the half-Heusler compound NiMnSb (in a half-Heusler, only one of the X sites is occupied), the majority-spin electrons are metallic whereas the minority-spin electrons are semiconducting [61]. This property has become known as 'half-metallicity'.

Further theoretical study of half-metallicity of Heusler alloys predicted that the total spin magnetic moment for Co-based full-Heusler compounds follows the well-known Slater-Pauling behaviour [11, 62] :

$$M_t = Z_t - 24,$$

where M_t is the total magnetic moment and Z_t is the number of valence electrons.

This special phenomenon is explained by Co-Co hybridization which forces the minority channel to contain an integer number of electrons [11]. Such half-metallic ferromagnets with complete spin polarization and a high Curie temperature of 985K [63] attracted researchers' attention to investigate them as a candidate for spintronic devices [64].

DFT calculations of Co_2MnSi indicate that an ideal crystal of Co_2MnSi is a typical full-Heusler alloy which has metallic majority channel while a gap exists

for minority channel [65,66]. The calculated total magnetic moment per primitive cell of 5μB strictly follows the Slater-Pauling behaviour. Further research showed that chemical disorder of Co_2MnSi, especially for Co antisites, will destroy the half-metallicity by a defect-induced peak in the DOS at the Fermi energy [67]. However, in most cases, the half-metallicity of an ideal Co_2MnSi crystal is robust on the basis of the results of calculations [68]. In addition, it is worth to notice that the intrinsic weak point of DFT methods may not be reliable for Co_2MnSi because of the transition metal elements Co and Mn with $3d$ electrons [25, 40]. Therefore, some calculations that go beyond standard DFT methods have also been applied to study Co_2MnSi. The results from a DFT+U calculation showed that the gap in minority DOS exists only with a relatively low effective Coulomb exchange interaction [69].

The experimental measurements of the magnetization of Co_2MnSi indicate an integer total magnetic moment of 5μB of Co_2MnSi which agrees well with the theoretical calculations [70, 71]. Despite a good agreement of magnetic moment between experiments and calculations, many researchers pointed that the spin polarization may be different from the theoretical predictions. The point-contact Andreev reflection measured by Ritchie*et al.* indicated that the spin polarization of Co_2MnSi is only 55% which much less than the theoretical calculations [72]. Considering that the surface effects like surface segregation might be the cause of such discrepancy, a large spin polarization of $93^{+7}_{-11}\%$ was measured at room temperature in the surface region of Co_2MnSi [12]. In line with the theoretical results, the presence of site disorder of Co_2MnSi is a possible explanation of the reduction of spin polarization. However, the inherent chemical disorder in Co_2MnSi crystals is difficult to avoid [70]. Neutron diffraction and X-ray-absorption fine-structure measurements (EXAFS) on bulk Co_2MnSi showed that Co-Mn antisite disorder is likely to happen because of the similarity of the size and electronic

structure between Co and Mn [73].

When talking about the electronic structure of metals, the Fermi surface has always played a very important role. However, the disorder and surface effects of Heusler alloy will significantly influence the measurements of the Fermi surface. Growing a high-quality single crystal Heusler alloys is known to be very challenging and it is even more difficult for Co_2MnSi [73].

Experimentally, traditional methods for measuring the Fermi surface, such as quantum oscillatory techniques or angle-resolved photoemission are similarly challenging. Indeed, no such results exist which suggests that the sample quality means that electron mean-free-paths are likely too short for quantum oscillations to be observed at reasonable temperatures and magnetic fields and that the samples are difficult to cleave making photoemission impossible. What is more, the DFT calculations for correlated $3d$ electrons in such compounds may not predict the correct Fermi surface. Therefore, it is very difficult to reproduce an accurate Fermi surface for Heusler alloys from both experiments and calculations [20, 74].

Recently, great progress has been made in using Compton scattering to discover the electronic structure of Co_2MnSi [9]. From the electron momentum distribution (EMD) it is possible to reconstruct the Fermi surface of Co_2MnSi with the method developed by Kontrym-Sznajd *et al.* [75]. However, the Fermi surface obtained from such Compton profile measurements is different from those predicted by DFT and DFT+U calculations [9] which motivates us to develop a new method to discover its properties theoretically.

In this work, we will focus on the differences between the Compton scattering experiments and the DFT local spin-density approximation (DFT-LSDA) calculations. We shall further see that a better description based on the GW approximation will lead to a different structure of the Fermi surface. The combination of Compton profile and GW methods provides a new powerful tool to discover the

Fermi surface of systems that beyond DFT.

5.2 Crystal structure

Co_2MnSi is one of the full-Heusler alloys which has the chemical formula of X_2YZ, where X and Y are transition metals and Z is a main group element. Such compounds crystallize in the cubic group $Fm\text{-}3m$(space group 225). The X atoms (Co) are located at the Wyckoff position $8c(1/4, 1/4, 1/4)$, the Y atoms occupy the $4a(0, 0, 0)$ position and Z atoms occupy the $4b(1/2, 1/2, 1/2)$ site. As shown in Figure 10, the $L2_1$ crystal structure of Co_2MnSi consists of four interpenetrating FCC lattices. The lattice parameters are shown in Table 4 [76].

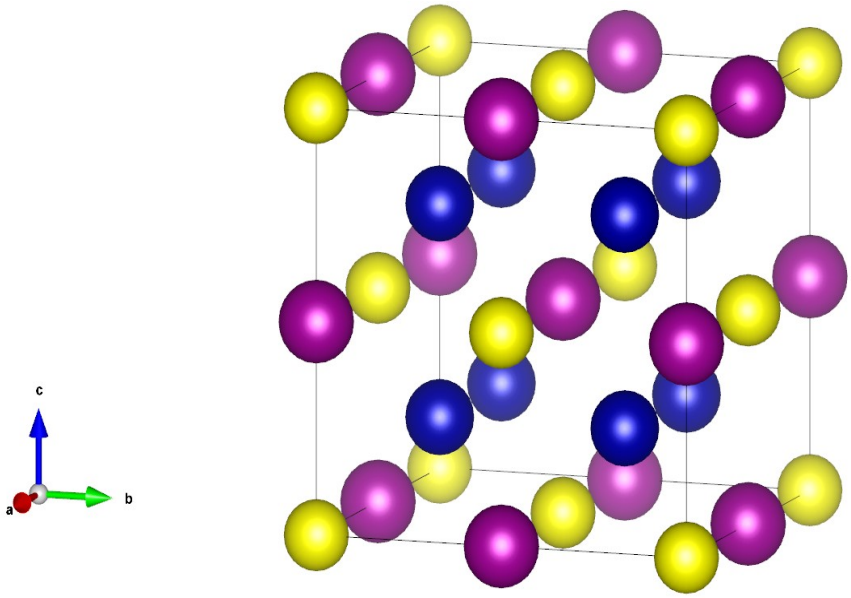

Figure 10: Crystal Structure of Co_2MnSi(conventional cell). Co atoms are shown as blue spheres, Mn atoms are purple and Si atoms are yellow.

X-ray diffraction measurements indicate that the sample has an integer stoichiometry with lattice constant equal to 5.654Å [9].

Space group	Fm-3m(No.225)
Lattice constant(Å)	5.654(5)
Wyckoff position of Co	(0.25 0.25 0.25)
Wyckoff position of Mn	(0.5 0.5 0.5)
Wyckoff position of Si	(0 0 0)

Table 4: Experimental lattice constants and positions of atoms of Co_2MnSi.

5.3 Compton scattering

Compton scattering was discovered by Arthur Holly Compton in 1923 and led to him winning the Nobel Prize for Physics in 1927 [77].The essence of Compton scattering is the inelastic scattering of photons (X-rays) with a charged particle (which is usually an electron). Experimentally, Compton scattering measures the EMD which contains the information about the Fermi surfaces of crystalline metals [21]. If we describe the scattering process together with energy and momentum conservation, the relation between the change of wavelength of photon and electron's momentum can be written as:

$$\begin{aligned} \omega_1 - \omega_2 &= \frac{1}{2}m\left[\boldsymbol{p} + \hbar(\boldsymbol{k_1} - \boldsymbol{k_2})\right]^2 - \frac{p^2}{2m} \\ &= \frac{\hbar^2|\boldsymbol{K}|^2}{2m} + \frac{\hbar\boldsymbol{K}\cdot p}{m}, \end{aligned} \tag{5.1}$$

where ω is the wavelength of the photon, p is the momentum of an electron and $\boldsymbol{K} = \boldsymbol{k}_1 - \boldsymbol{k}_2$ is the scattering vector [78]. Then we can get:

$$\boldsymbol{J}(p_z) = \iint_{p_x p_y} n(p_x, p_y, p_z) dp_x dp_y, \tag{5.2}$$

where $\boldsymbol{J}(p_z)$ is usually called the Compton profile and $n(\boldsymbol{p})$ is the EMD in p space. Owing to the periodic nature of crystals that was discussed in Chapter 2

(Equation 2.13), the EMD in p space can be expreesed as:

$$\rho(\boldsymbol{p}) = \sum_{\boldsymbol{k},\boldsymbol{G}} \delta(\boldsymbol{p} - \boldsymbol{k} - \boldsymbol{G})|a(\boldsymbol{k} + \boldsymbol{G})|^2 \tag{5.3}$$

where $\boldsymbol{G}$ is a reciprocal lattice vector and $a(+\boldsymbol{G})$ is the Fourier coefficient. Consequently, the 3D-EMD measurement in $\boldsymbol{p}$ space can be folded back into the first BZ. This process is based on the so-called LCW (Lock-Crisp-West) technique [79]. The EMD in k space can be then written as:

$$\rho(\boldsymbol{k}) = \sum_{G'} \rho(\boldsymbol{p}) \tag{5.4}$$

However, the momentum distribution in the Compton profile is projected onto p_z axis which means that more information is needed if the aim is to reconstruct the full 3D Fermi surface. Kontrym-Sznajd *et al.* presented a method to reconstruct the Fermi surface with the data of Compton scattering [80]. In practice, seven so-called special directions were chosen to be measured, representing a trade-off between a large enough number of directions and the statistical precision of each one. Thus, the full 3D momentum distribution can be obtained from the Compton scattering experiments. Details of the reconstruction procedure can be found in Ref [9].

5.4 Density functional theory calculation of Co_2MnSi

The electronic structure of Co_2MnSi was calculated by the Elk code The DFT-LSDA [81] calculations were chosen as the starting point for discovering the electronic structure of Co_2MnSi. All of the calculations are based on the experimental crystal structure parameters. Atomic units are used in the following calculation (including the GW calculations).

5.4.1 Computational details

The ground-state calculation of Co_2MnSi was well converged with a k-point grid of 24×24×24 (leading to 413 irreducible k points in first BZ) and $(G + K)_{max} = 8.5/R_{MT}$, where the MT radii for Co, Mn and Si were 2.2883 a.u., 2.8883 a.u. and 2.2000 a.u., respectively. The number of valence electrons for Co, Mn and Si were 15, 15 and 4, respectively which leads to 49 valence electrons in total while the number of empty states was 56 (14 empty states for each atom in the primitive cell). The spin-orbit coupling was usually considered as a negligible ingredient of Co_2MnSi due to the low atom number of these three elements. It was found that for the DFT-LSDA calculation, inclusion of spin-orbit coupling does not significantly change the electronic sturcture, especially for the band structure and topology of Fermi surfaces.

The temperature of the calculated system is 300K, which is commensurate with the temperature of the experimental measurements but well below the Curie temperature (985K). A magnetic field was applied along [001] direction at the beginning of the calculation to break the degeneracy, but it was gradually removed during the convergence. The calculated total magnetic moment is 5.00μB, which is in good agreement with previous calculations and experiments.

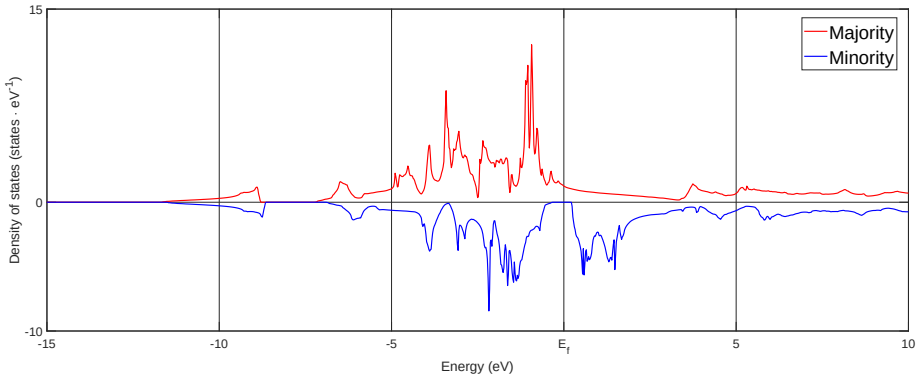

Figure 11: Spin-resolved total density of states of Co_2MnSi.

The calculated total density of states (TDOS) of Co_2MnSi is shown in Figure 11. It is very clear that a gap exists in the minority DOS which indicates the half-metallicity of Co_2MnSi. An energy integration up to the Fermi energy of the majority DOS gives 27 electrons while only 22 for minority DOS which exactly fulfills the Slater-Pauling rule.

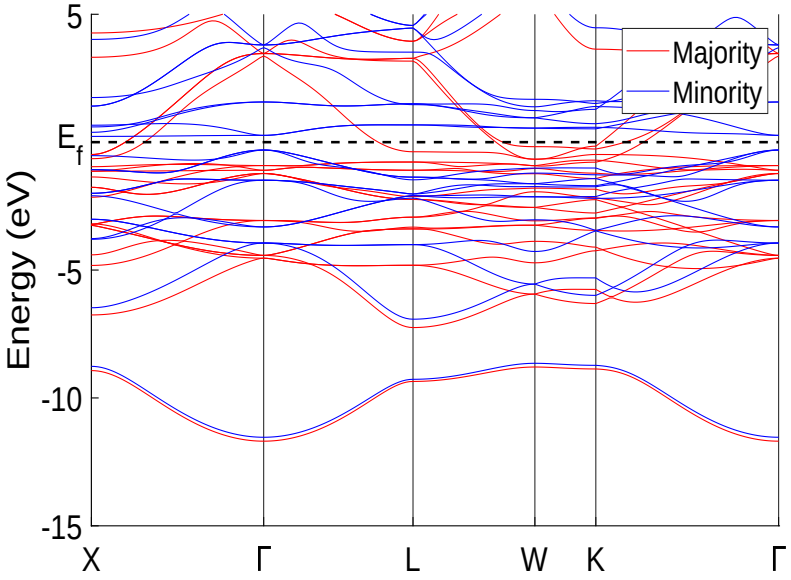

(a)

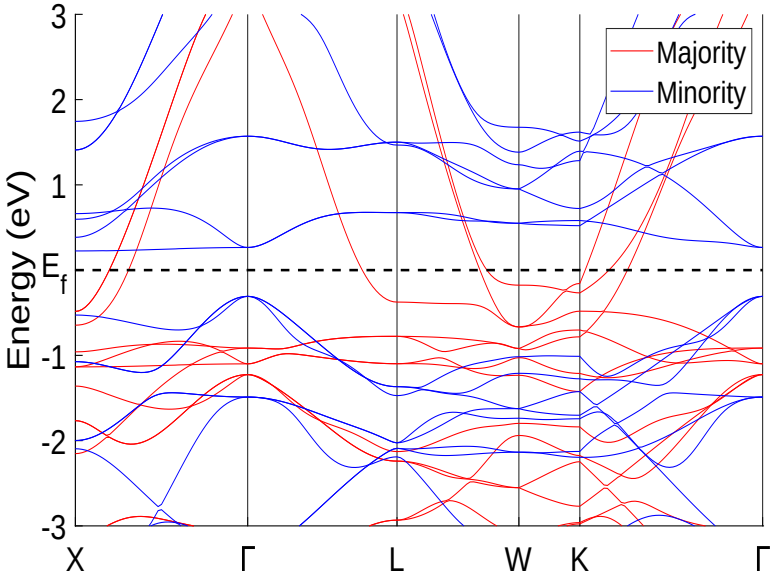

(b)

Figure 12: Band structure of Co_2MnSi.

The band structure of ferromagnetic Co_2MnSi is shown in Figure 12. It is clear from Figure 12 (b) that there is a direct gap for minority electrons at the Γ point

while the majority bands cross the Fermi level. What is more, along the high symmetry path from K to Γ, three bands cross the Fermi level which indicates three sheets of Fermi surfaces.

The Fermi surfaces of Co_2MnSi are shown in Figure 13. These three sheets of Fermi surfaces are the result of the occupation change of majority electron bands as they cross the Fermi energy. It can be found that the last two sheets of Fermi surface that are shown in Figure 13(b) and 13(c) are very similar, while the first one in Figure 13 (a) is close to the shape of the boundary of the first BZ. However, comparing with the experimental Fermi surfaces [9], only the third sheet is similar while the second one and the first one are different from the experiments [**?**]. We shall further see in the next two sections that a calculation which more properly treats the electron correlations in Co_2MnSi may lead to a different Fermi surface topology.

5.5 Electron correlations in Co_2MnSi

In the DFT framework, different functionals are designed to calculate the exchange-correlation interactions. However, a precise exchange-correlation functional is difficult to evaluate as discussed before. Recent work has also indicated that Co_2MnSi and other Co-based Heusler alloys may be the host of strong electron correlations [69, 82–84]. Therefore, it is necessary to introduce a new method to properly describe the electron correlations in Co_2MnSi.

5.6 GW calculations of Co_2MnSi

Comparing with the LSDA results, the reconstructed Fermi surface from Compton profile shows a different structure in first BZ, which indicates that the inherent inadequacies of DFT may lead to an inaccurate description of the Fermi surface

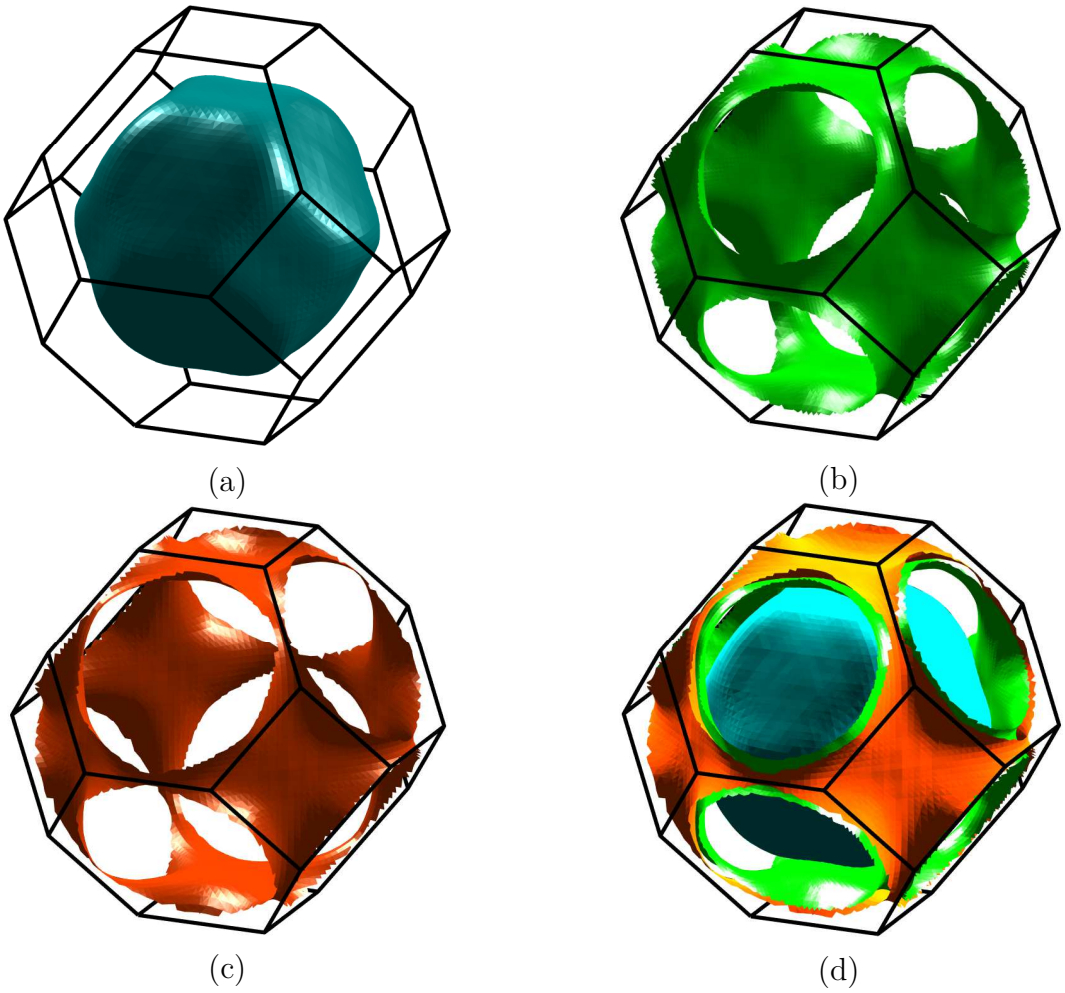

Figure 13: Fermi surfaces from LSDA calculation are shown in subfigure (a-c), the combination of three sheets shown in (d). There is no minority band crossing the Fermi level which indicates a 100% spin polarization.

of Co_2MnSi. In order to correct such discrepancy, the single shot G^0W^0 method was used to calculate the Fermi surfaces.

5.6.1 Computational details

The G^0W^0 calculation was based on a previous ground-state DFT-LSDA calculation. The energy tolerance for the self-consistent DFT iteration was 10^{-8} Ha. The maximum angular momentum cut-off for the APW functions and for the MT density and potential were 12 and 8, respectively. The maximum Matsubara frequency of self-energy calculation was 8 Ha. In order to balance the computation costs, only the diagonal terms of self-energy were computed. The N-point-Padé Analytic continuation procedure is performed [1, 47]. Although we have made a compromise between the quality and the computation cost, it is still an extremely heavy calculation even for a high-performance computer. This job took about 300000 core-hours (1400 cores for 10 days).

5.6.2 Results and discussion

From the results of GW calculation, the electron distribution in first BZ can be reconstructed by integrating the spectral function of each irreducible k-point with Equation 4.30. In contrast with previous calculations for the simple metals, the numerical noise from the analytical continuation problem is more visible for this complex alloy as shown in Figure 14. It should be noted that the single-shot G^0W^0 calculation does not satisfy the conservation law for particle number which will lead to electron missing at some particular k points and may change the volume of the Fermi isosurfaces. But this violation was usually small [85, 86] so it won't significantly change the determination of the Fermi energy and the structure of the Fermi surfaces. What is more, as mentioned above, the analytical continuation

procedures may also create numerical noise randomly which will also technically lead to the violation of the total particle number. Thus, a 3-D Gaussian convolution with FWHM of 0.1 a.u. is applied to both DFT-LSDA and GW results to filter the noise. The convoluted GW results are further scaled to the expected number of valence electrons(from 48 to 51). All the following results are based on the convoluted data(except where noted). The convoluted results are shown in Figure 15 comparing with the data of our experiments. It can be found that the occupation distribution is clear after convolution while the main features were kept. In addition, it should be noticed that the color of the point has not been scaled in the same range in Figure 15.

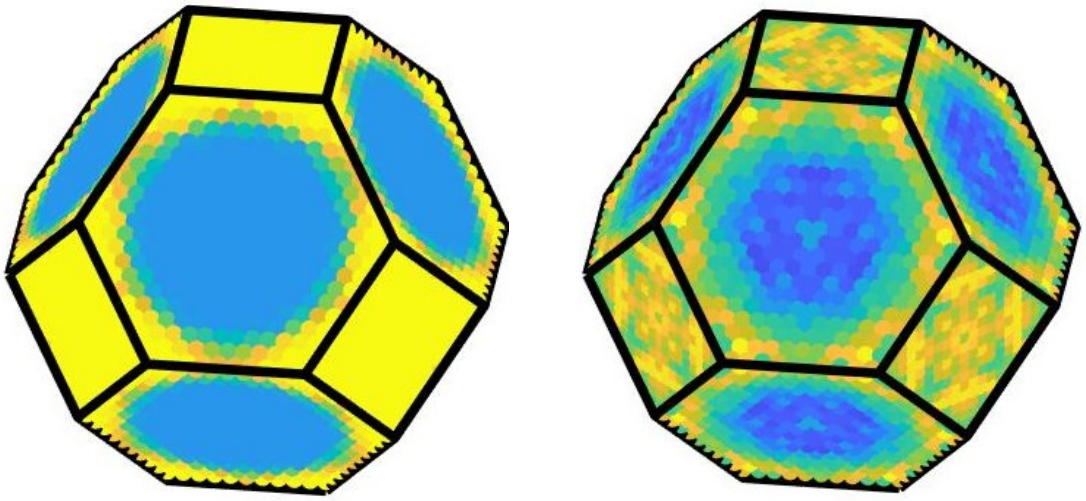

(a) (b)

Figure 14: Occupation distribution of first BZ. High occupancy k points are shown with yellow while low occupancy k points are in blue. The solid black lines are the boundary of the first BZ. Only the points at first BZ boundary are shown.(a) unconvoluted DFT-LSDA calculation. (b) unconvoluted GW calculation.

As mentioned before, the Fermi surface is defined as being where the occupation number of the electrons suddenly changes. But in practice, the distribution of electrons in momentum space is no longer a precise step function due to the

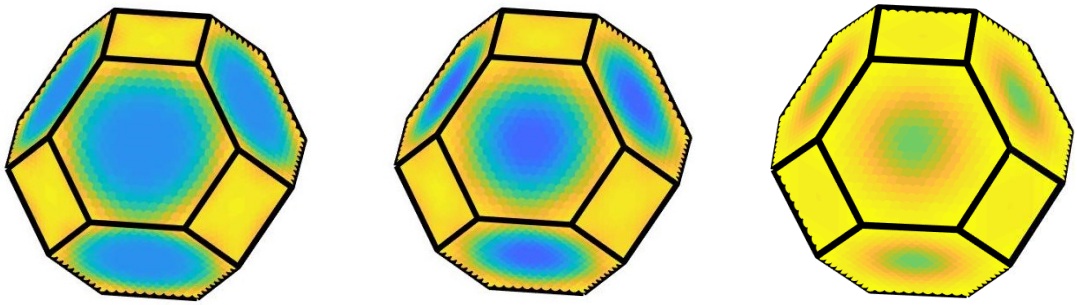

(a) (b) (c)

Figure 15: Convoluted occupation distribution of first BZ. High occupancy k points are shown with yellow. Low occupancy k points are in blue. The solid black lines are the boundary of the first BZ. Only the points at first BZ boundary are shown. (a)Convoluted DFT+LSDA calculation. (b) Convoluted GW calculation (c)Experimental data.

excitation of the quasi-particles. Thus, the isolevel of the contour is difficult to define. Such smearing of the electron distribution is visible in Figure 16. Note that the convoluted GW of that figure are from the raw GW results which has noise. The GW results (both convoluted and unconvoluted) are relatively smooth, while LSDA calculation shows a sharp change of the occupation which indicates the existence of the Fermi surface. It can be found from Figure 16 (a) along W-W' direction, such a smooth variation leads to a narrower 'valley'. What is more, the number of states at K point is 50 for GW calculation while DFT-LSDA result is 51. This will lead to a small difference of the third sheet of Fermi surface between DFT-LSDA and GW results as shown in Figure 20 (f) and (c). It should be noticed that even after scaled, the number of electrons at some points of GW calculation are still slightly lower than that from DFT. This is because of the noise that from the analytical continuation.

A further comparison of the 2D-EMD is shown in Figure 18. The slices are from the convoluted 3D-EMD as shown in Figure 15. The positions of these slices are shown in Figure 17 schematically. The variations of the occupation of electrons

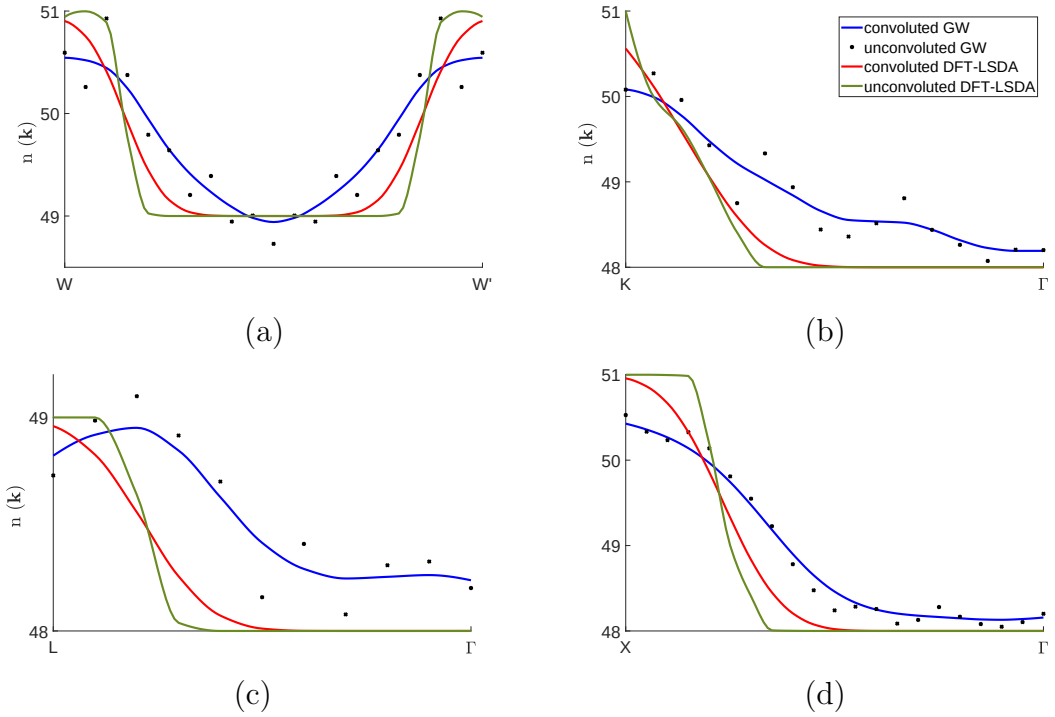

Figure 16: The occupation distribution along W-W'(a), K-Γ(b), L-Γ (c) and X-Γ (d). The high symmetry points are shown in Figure 17. 1-D Gaussian convolution with FWHM of 0.14 a.u. is used to simulate the experimental resolution function. Please note that the GW and DFT results are based on the original results as shown in Figure 14(a) and (b) which are not convoluted. The blue lines are the convoluted GW calculation. The unconvoluted GW results are shown in black points, convoluted DFT-LSDA results are shown in red while unconvoluted DFT-LSDA is shown in green.

are clear from Figure 18. In the (0 0 0) plane (Figure 18 (a), (c),(e)), the central part where there is lower occupancy, which is enclosed by the first sheet of Fermi surface, has a larger size for DFT-LSDA calculation, while the GW calculation has fixed that discrepancy to some extent. However, the first sheet from GW is still slightly bigger than that from experiments as shown in Figure 18 (d), whose central region in blue is, in fact, the top part of the first sheet. A good agreement between GW calculation and experiments can be found at the plane (0 0 1/2) along W-W' direction. DFT-LSDA calculation shows a wider 'neck', which cor-

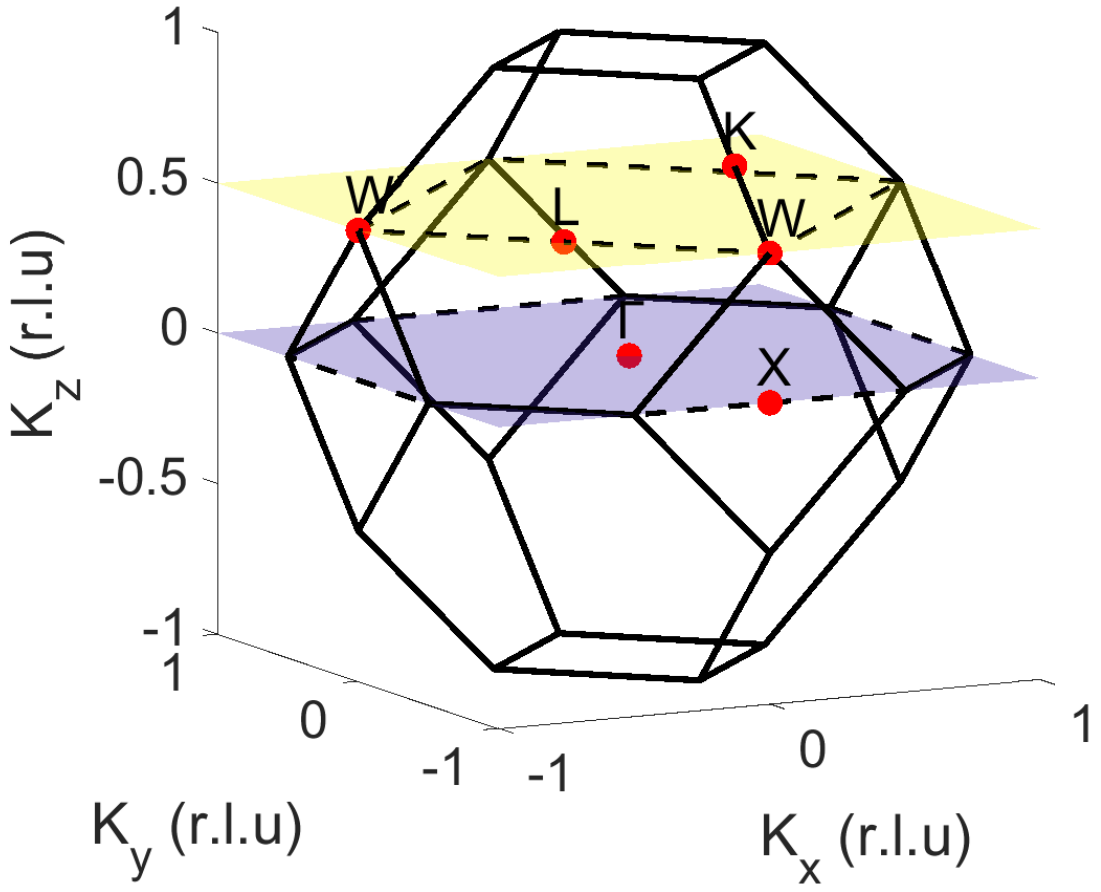

Figure 17: The first BZ of Co_2MnSi. The pruple plane is the (0 0 1) plane through the Γ point, while the yellow plane is the (0 0 1) plane shifted by π/a(0.5 r.l.u) along the [001] direction from Γ point. The red points are the high symmetry points.

responding to the 'valley' in Figure16 (a), along that direction and consequently lead to two similar sheets of Fermi surface as shown in Figure 20 (b) and (c)(green and orange). However, that 'neck' is much narrower for both GW calculation and experiments. It should be noticed that from Figure 18 (b), a different orientation of the first sheet can be found when comparing with DFT-LSDA results. It is, in fact, a different shape of the first sheet of Fermi surface which is visible in Figure 20(a) and (d).

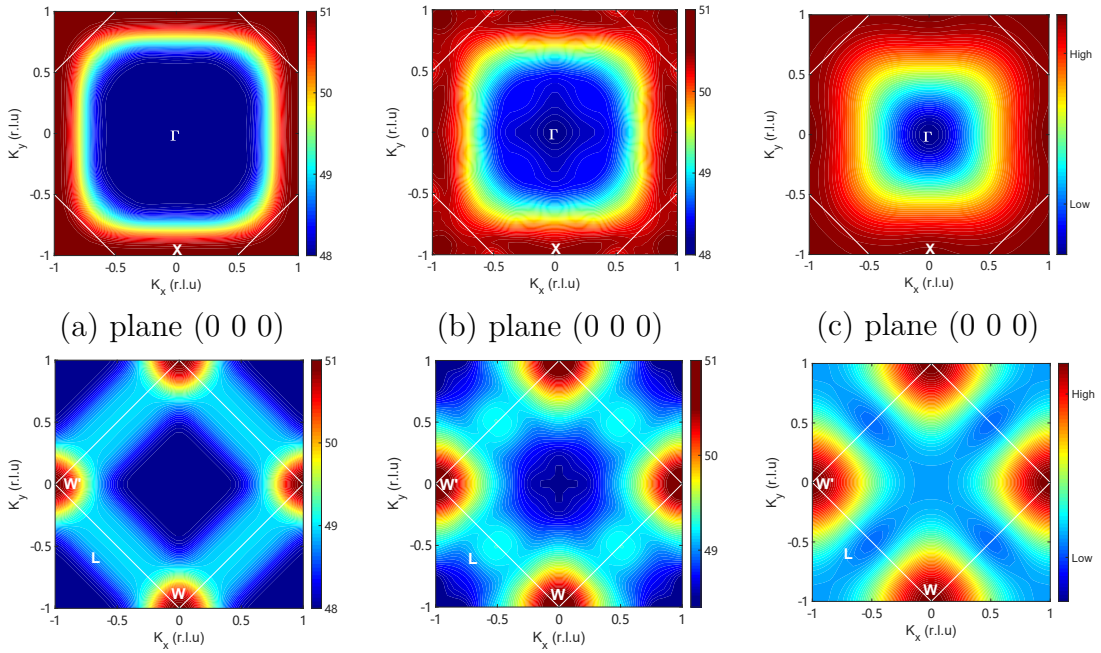

(a) plane (0 0 0) (b) plane (0 0 0) (c) plane (0 0 0)

(d) plane (0 0 1/2) (e) plane (0 0 1/2) (f) plane (0 0 1/2)

Figure 18: Slices of 2D-EMD in the first BZ. The slices are from the convoluted 3D-EMD as shown in Figure 15. White lines are the BZ boundary of each slice. (a) and (d) are from LSDA calculations, (b) and (e) are from GW calculations, (c) and (f) are from the experimental data.

Different from Li and Cu, it is more difficult to directly find the isovalue of the Fermi surfaces. As a multisheet material, Co_2MnSi is expected to have three different sheets of Fermi surface. Therefore, the gradient of the EMD is required to straight find the structure of the Fermi surfaces. As shown in Figure 19, the 2D

gradient of the EMD directly indicates the shape and the position of the Fermi surfaces. It can be also found from Figure 19(b) (e), the regions with warm color are localized which indicates a robust Fermi surface. By comparing Figure 18 19, the isovalues of the first sheet is 48.5, 49.4 for the second sheet and 50.6 for the third one.

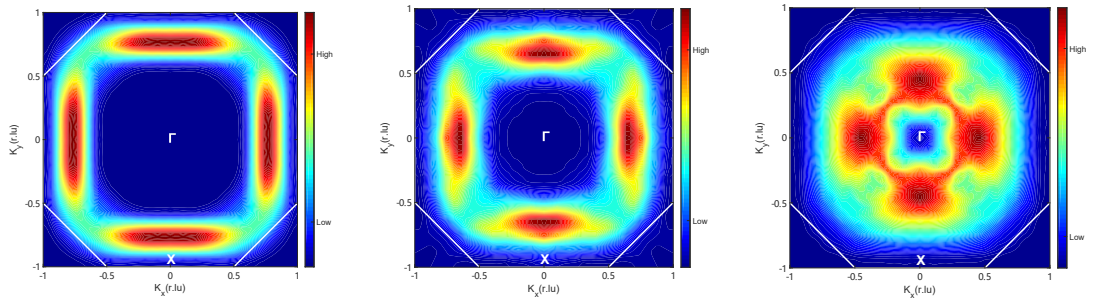

(a) plane (0 0 0) (b) plane (0 0 0) (c) plane (0 0 0)

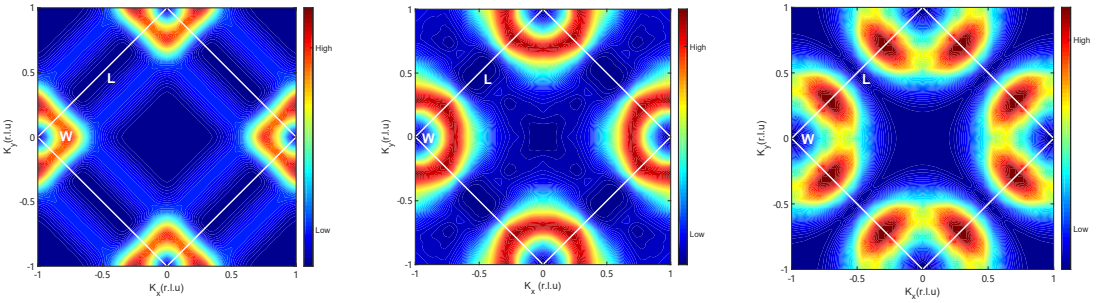

(d) plane (0 0 1/2) (e) plane (0 0 1/2) (f) plane (0 0 1/2)

Figure 19: The gradient of 2D-EMD. The slices are from the convoluted 3D-EMD as shown in Figure 15. White lines are the BZ boundary of each slice. (a) and (d) are from LSDA calculations, (b) and (e) are from GW calculations, (c) and (f) are from the raw experimental data. The area with warm colour directly indicates the positions of Fermi surfaces.

The Fermi surfaces from the DFT-LSDA calculation, GW calculation and Compton scattering experiments are shown in Figure 20. The GW calculation shows a surprisingly good agreement with experiments. The third sheet of the Fermi surface of the DFT-LSDA calculation, GW calculation and experiment are

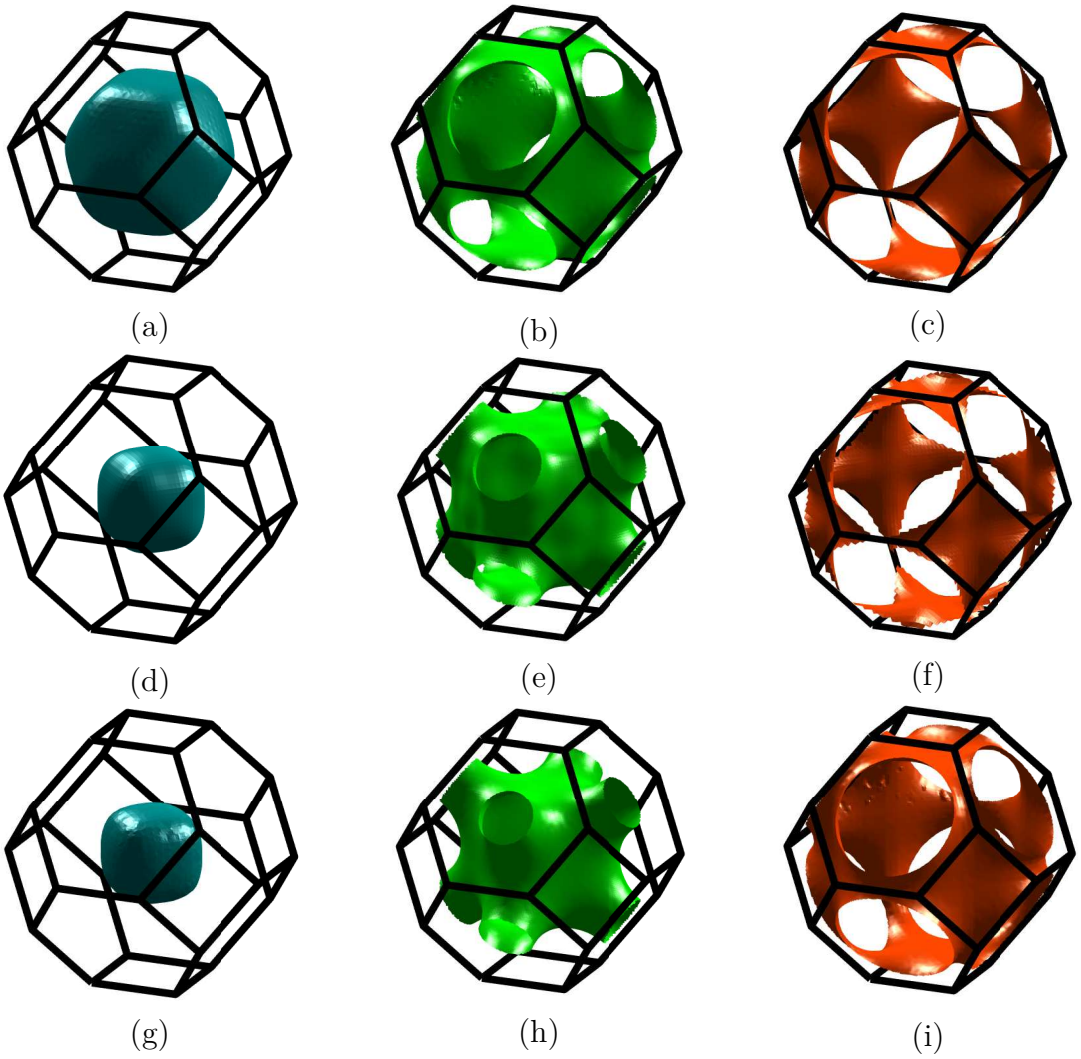

Figure 20: Fermi surfaces that from DFT-LSDA calculation are shown in subfigure (a-c), the GW calculations are shown in (d-f), the Compton scattering experiments are shown in (g-i). All the Fermi surfaces are contoured from the convoluted data.

basically the same. However, the third sheet of GW calculation is discontinuous at K point This can be directly found from Figure 16 (b). The second sheet from GW calculation and experiments show a similar shape with a narrow 'neck' at the boundary of the first BZ, while the DFT-LSDA calculation shows a wider 'neck' and larger volume of the Fermi surface which is different in both the GW calculation and the experimental data. For the first sheet, as mentioned before, the DFT-LSDA and the GW calculation show a different shape of the Fermi surface. It is clear that the first sheet of the GW and the experiments are both cubic-like, while the result of DFT-LSDA has the same shape as the first BZ. The agreement between GW results and experiments indicates that the correlations of electrons in Co_2MnSi may play an important role in determining the structure of the Fermi surface.

5.6.3 Summary and conclusions

With 100% spin polarization and very high Curie temperature of 985K, Co_2MnSi has been seen as a candidate of spintronic devices and attracted widespread attention. In this work, a traditional DFT-LSDA calculation shows that Co_2MnSi is a half-metal, with a direct minority gap exist at the Γ point, in agreement with previous work. However, the DFT-LSDA prediction of the Fermi surfaces of Co_2MnSi is different from that indicated by Compton scattering experiments. In order to try to correct this difference, a single-shot GW calculation was applied to reconstruct the Fermi surfaces from the quasi-article spectral functions. Owing to the analytical continuation procedures and the limitation of the computers, the structure of the Fermi surfaces of a multi-sheet system is very difficult to reproduce from GW spectral function in practice. However, the results from the GW calculation are still encouragingly more consistent with the experiments. It can be found from the gradients in Figure19, the Fermi surfaces are still very localized

when comparing with the experiments. The discrepancy between DFT-LSDA and Compton scattering experiments is partially corrected by our GW calculation. It indicates that correlations of electrons in Co_2MnSi cannot be neglected. However, our GW calculation shows that the number electrons at some k points are lower than 48 which will lead to the broken of half-metallicity. This may due to the nature of the single-shot G^0W^0 method in which particle number is not conserved. Consequently, the single-shot GW results have been scaled to match the number of electrons from the DFT-LSDA calculation.

What is more, the smearing of occupation distribution has previously been considered to be a result of disorders and defects. Our calculations, with the description of quasi-particle theory, suggest that the electron correlations would be one of the reasons as well.

6 Conclusion

The Fermi surface is seen as one of the most important concepts of condensed matter physics. It is defined as the interface between occupied and unoccupied states in k space. Therefore, the Fermi surface is also an unique characteristic of metals which has at least one band that crosses the Fermi energy and leads to a sudden change of the number of occupied states in k space. The standard theoretical method for predicting the Fermi surface is based on DFT. However, due to the exchange-correlation associated with the electrons, it is difficult to describe the electronic structure accurately in real materials. To solve this problem, a series of new methods were proposed such as DFT+U and GW method.

The single-shot GW calculations were firstly applied to simple materials in Chapter 4 for studying the theory and testing the performance of GW calculation in the Elk code. The calculated DOS of insulators and semiconductors successfully improved the deficiencies of the DFT-LDA calculation. The reconstruction of the Fermi surface of metals is based on the (energy) integration of spectral functions. A test of the Fermi surface of simple metals discussed in Chapter 4 proves that this approach is reasonable. The Fermi surfaces of Li and Cu from GW calculations are in agreement with previous calculations and experiments.

The motivation for this dissertation is to address the discrepancy between the experimental Fermi surfaces and the calculated Fermi surfaces of Co_2MnSi. From Compton scattering experiments, the EMD of materials' electrons in k space can be measured directly from the Compton profiles. However, it was found [9] that the experimental Fermi surfaces are not well described by either a DFT-LSDA calculation or the DFT+U calculation, possibly due to the inadequate description of electron correlations in Co_2MnSi. Consequently, using the same method of reconstructing the Fermi surface of Li and Cu, a single-shot GW calculation was performed to attempt to correct the DFT-LSDA results of Co_2MnSi.

In Chapter 5, a high-quality DFT-LSDA calculation was first performed to provide the orbitals of the 'non-interacting' Green's function that is described in Equation 4.27. From the results of the DFT-LSDA calculation, the total magnetic moment is 5.00μB which is in line with magnetic Compton scattering experiments [9]. The band structure and the density of states also indicate that Co_2MnSi is a half-metal with 100% spin polarization. However, the calculated Fermi surfaces are different from the experiments.

The single-shot GW calculation was subsequently applied to try to correct this discrepancy. It can be found that the single-shot GW calculation shows an improved agreement with the Compton scattering experiments. But from the results of the single-shot GW calculation, a small hole pocket was found to exist at the Γ point of the first BZ. It is probably owing to the nature of the non-self-consistent GW method which does not satisfy the particle number conservation and lead to an electron missing. In addition, the numerical problem of analytical continuation may also lead to a deviation of the number of particles. Therefore, future work will focus on self-consistent GW or half-self-consistent GW calculation(which the loop is only based on Green's function G while W keep same.) and further extend to other relative methods such as DMFT.

In conclusion, the GW method is one of the most powerful tools for studying the electronic structures of materials, which gives a percise description of the exchange-correlation interactions beyond DFT. Together with the high-resolution Compton scattering technique, it is possible to discover the Fermi surface of complex materials both theoretically and experimentally.

References

[1] Kay Dewhurst, Sangeeta Sharma, L Nordstrom, F Cricchio, F Bultmark, H Gross, C Ambrosch-Draxl, C Persson, C Brouder, R Armiento, et al. The elk fp-lapw code. *ELK, http://elk.sourceforge.net*, 2016.

[2] JE Hirsch. Spin hall effect. *Physical Review Letters*, 83(9):1834, 1999.

[3] Paul Drude. Zur elektronentheorie der metalle. *Annalen der Physik*, 306(3):566–613, 1900.

[4] SB Dugdale. Life on the edge: a beginner's guide to the fermi surface. *Physica Scripta*, 91(5):053009, 2016.

[5] Walter Kohn and Lu Jeu Sham. Self-consistent equations including exchange and correlation effects. *Physical review*, 140(4A):A1133, 1965.

[6] David Sholl and Janice A Steckel. *Density functional theory: a practical introduction*. John Wiley & Sons, 2011.

[7] Axel D Becke. Density functional calculations of molecular bond energies. *The Journal of Chemical Physics*, 84(8):4524–4529, 1986.

[8] Jörg Schäfer, M Hoinkis, Eli Rotenberg, Peter Blaha, and R Claessen. Fermi surface and electron correlation effects of ferromagnetic iron. *Physical Review B*, 72(15):155115, 2005.

[9] Thomas Edward Millichamp. *A bulk half-metal and an unexpected Fermi surface*. PhD thesis, University of Bristol, 2017.

[10] Fr Heusler. Über Manganbronze und über die Synthese magnetisierbarer Legierungen aus unmagnetischen Metallen. *Angewandte Chemie*, 17(9):260–264, 1904.

[11] I Galanakis, PH Dederichs, and N Papanikolaou. Slater-Pauling behavior and origin of the half-metallicity of the full-Heusler alloys. *Physical Review B*, 66(17):174429, 2002.

[12] M Jourdan, J Minár, J Braun, A Kronenberg, S Chadov, B Balke, A Gloskovskii, M Kolbe, HJ Elmers, G Schönhense, et al. Direct observation of half-metallicity in the Heusler compound $Co_2MnSi. Naturecommunications, 5 : 3974, 2014.$

[13] Lars Hedin. New method for calculating the one-particle green's function with application to the electron-gas problem. *Physical Review*, 139(3A):A796, 1965.

[14] Ferdi Aryasetiawan and Olle Gunnarsson. The gw method. *Reports on Progress in Physics*, 61(3):237, 1998.

[15] W Friedrich, P Knipping, and Mvon Laue. Sitzungsber. math. phys. kl. k. *Bayer. Akad. Wiss. München*, pages 303–322, 1912.

[16] Charles Kittel et al. *Introduction to solid state physics*, volume 8. Wiley New York, 1976.

[17] Joseph John Thomson. Xl. cathode rays. *The London, Edinburgh, and Dublin Philosophical Magazine and Journal of Science*, 44(269):293–316, 1897.

[18] L Onsager. Interpretation of the de haas-van alphen effect. *The London, Edinburgh, and Dublin Philosophical Magazine and Journal of Science*, 43(344):1006–1008, 1952.

[19] P Richard, T Sato, K Nakayama, T Takahashi, and H Ding. Fe-based superconductors: an angle-resolved photoemission spectroscopy perspective. *Reports on progress in physics*, 74(12):124512, 2011.

[20] Josef A Weber, Andreas Bauer, Peter Böni, Hubert Ceeh, Stephen B Dugdale, David Ernsting, Wolfgang Kreuzpaintner, Michael Leitner, Christian Pfleiderer, and Christoph Hugenschmidt. Spin-Resolved Fermi Surface of the Localized Ferromagnetic Heusler Compound Cu2MnAl Measured with Spin-Polarized Positron Annihilation. *Physical review letters*, 115(20):206404, 2015.

[21] Y Sakurai, Y Tanaka, A Bansil, S Kaprzyk, AT Stewart, Y Nagashima, T Hyodo, S Nanao, H Kawata, and N Shiotani. High-resolution Compton scattering study of Li: Asphericity of the Fermi surface and electron correlation effects. *Physical review letters*, 74(12):2252, 1995.

[22] LD Landau. The theory of a fermi liquid. *Soviet Physics Jetp-Ussr*, 3(6):920–925, 1957.

[23] Evgenii Mikhailovich Lifshitz and Lev Petrovich Pitaevskii. *Statistical physics: theory of the condensed state*, volume 9. Elsevier, 2013.

[24] Lev Davidovich Landau and Evgenii Mikhailovich Lifshitz. *Quantum mechanics: non-relativistic theory*, volume 3. Elsevier, 2013.

[25] John P Perdew. Density functional theory and the band gap problem. *International Journal of Quantum Chemistry*, 28(S19):497–523, 1985.

[26] Harald Ibach and Hans Lüth. Dielectric properties of materials. In *Solid-State Physics*, pages 371–418. Springer, 2009.

[27] Pierre Hohenberg and Walter Kohn. Inhomogeneous electron gas. *Physical review*, 136(3B):B864, 1964.

[28] Mel Levy. Electron densities in search of hamiltonians. *Physical Review A*, 26(3):1200, 1982.

[29] John C Slater. A simplification of the hartree-fock method. *Physical review*, 81(3):385, 1951.

[30] Teepanis Chachiyo. Communication: Simple and accurate uniform electron gas correlation energy for the full range of densities, 2016.

[31] Seymour H Vosko, Leslie Wilk, and Marwan Nusair. Accurate spin-dependent electron liquid correlation energies for local spin density calculations: a critical analysis. *Canadian Journal of physics*, 58(8):1200–1211, 1980.

[32] T. Asada and K. Terakura. Cohesive properties of iron obtained by use of the generalized gradient approximation. *Phys. Rev. B*, 46:13599–13602, Nov 1992.

[33] John P. Perdew, Kieron Burke, and Matthias Ernzerhof. Generalized gradient approximation made simple. *Phys. Rev. Lett.*, 77:3865–3868, Oct 1996.

[34] Stefan Bl ugel and Gustav Bihlmayer. Full-potential linearized augmented planewave method. 2006.

[35] JC Slater. Energy band calculations by the augmented plane wave method. *Advances in quantum chemistry*, 1:35, 1964.

[36] David Singh. Ground-state properties of lanthanum: Treatment of extended-core states. *Physical Review B*, 43(8):6388, 1991.

[37] O Krogh Andersen. Linear methods in band theory. *Physical Review B*, 12(8):3060, 1975.

[38] Elisabeth Sjöstedt, Lars Nordström, and DJ Singh. An alternative way of linearizing the augmented plane-wave method. *Solid state communications*, 114(1):15–20, 2000.

[39] Antoine Georges, Gabriel Kotliar, Werner Krauth, and Marcelo J Rozenberg. Dynamical mean-field theory of strongly correlated fermion systems and the limit of infinite dimensions. *Reviews of Modern Physics*, 68(1):13, 1996.

[40] Lars Hedin. On correlation effects in electron spectroscopies and the GW approximation. *Journal of Physics: Condensed Matter*, 11(42):R489, 1999.

[41] Mark S Hybertsen and Steven G Louie. First-principles theory of quasiparticles: calculation of band gaps in semiconductors and insulators. *Physical review letters*, 55(13):1418, 1985.

[42] Xiao-Gang Wen. *Quantum field theory of many-body systems: from the origin of sound to an origin of light and electrons*. Oxford University Press on Demand, 2004.

[43] Christoph Friedrich and Arno Schindlmayr. Many-body perturbation theory: the gw approximation. *NIC Series*, 31:335, 2006.

[44] VP Zhukov, F Aryasetiawan, EV Chulkov, and PM Echenique. Lifetimes of quasiparticle excitations in 4 d transition metals: Scattering theory and lmto-rpa-gw approaches. *Physical Review B*, 65(11):115116, 2002.

[45] Lars Hedin. Electron correlation: keeping close to an orbital description. *International Journal of Quantum Chemistry*, 56(5):445–452, 1995.

[46] Martin M Rieger, L Steinbeck, ID White, HN Rojas, and RW Godby. The gw space-time method for the self-energy of large systems. *Computer Physics Communications*, 117(3):211–228, 1999.

[47] HJ Vidberg and JW Serene. Solving the eliashberg equations by means ofn-point padé approximants. *Journal of Low Temperature Physics*, 29(3-4):179–192, 1977.

[48] Claudia Ambrosch-Draxl and Jorge O Sofo. Linear optical properties of solids within the full-potential linearized augmented planewave method. *Computer Physics Communications*, 175(1):1–14, 2006.

[49] AV Kurdyumov, VL Solozhenko, and WB Zelyavski. Lattice parameters of boron nitride polymorphous modifications as a function of their crystal-structure perfection. *Journal of applied crystallography*, 28(5):540–545, 1995.

[50] ME Straumanis and EZ Aka. Precision determination of lattice parameter, coefficient of thermal expansion and atomic weight of carbon in diamond1. *Journal of the American Chemical Society*, 73(12):5643–5646, 1951.

[51] ME Straumanis and Jayant S Shah. Low temperature lattice parameters and expansion coefficients of ai2au and lif gruneisen constants of lif. *Zeitschrift für anorganische und allgemeine Chemie*, 391(1):79–85, 1972.

[52] B Holm and Ulf von Barth. Fully self-consistent gw self-energy of the electron gas. *Physical Review B*, 57(4):2108, 1998.

[53] Andrey Kutepov, Sergey Y Savrasov, and Gabriel Kotliar. Ground-state properties of simple elements from gw calculations. *Physical Review B*, 80(4):041103, 2009.

[54] Michael P Surh, Steven G Louie, and Marvin L Cohen. Quasiparticle energies for cubic bn, bp, and bas. *Physical Review B*, 43(11):9126, 1991.

[55] Eric L Shirley, Louis J Terminello, John E Klepeis, and Franz J Himpsel. Detailed theoretical photoelectron angular distributions for lif (100). *Physical Review B*, 53(15):10296, 1996.

[56] RWG Wyckoff. Cubic closest packed, ccp, structure. crystal structures, vol. 1, 7, 1963.

[57] Howard E Swanson, Eleanor Tatge, and Ruth K Fuyat. Standard x-ray diffraction powder patterns. 1953.

[58] F Aryasetiawan. Self-energy of ferromagnetic nickel in the gw approximation. *Physical Review B*, 46(20):13051, 1992.

[59] L Oberli, AA Manuel, R Sachot, P Descouts, and M Peter. Fermi surface of lithium studied by positron annihilation. *Physical Review B*, 31(9):6104, 1985.

[60] Alfred Brian Pippard. An experimental determination of the fermi surface in copper. *Phil. Trans. R. Soc. Lond. A*, 250(979):325–357, 1957.

[61] RA De Groot, FM Mueller, PG Van Engen, and KHJ Buschow. New class of materials: half-metallic ferromagnets. *Physical Review Letters*, 50(25):2024, 1983.

[62] J Kübler. First principle theory of metallic magnetism. *Physica B+ C*, 127(1-3):257–263, 1984.

[63] PJ Brown, Klaus-Ulrich Neumann, PJ Webster, and KRA Ziebeck. The magnetization distributions in some Heusler alloys proposed as half-metallic ferromagnets. *Journal of Physics: Condensed Matter*, 12(8):1827, 2000.

[64] Claudia Felser, Gerhard H Fecher, and Benjamin Balke. Spintronics: a challenge for materials science and solid-state chemistry. *Angewandte Chemie International Edition*, 46(5):668–699, 2007.

[65] S Amari, R Mebsout, S Méçabih, B Abbar, and B Bouhafs. First-principle study of magnetic, elastic and thermal properties of full Heusler Co2MnSi. *Intermetallics*, 44:26–30, 2014.

[66] I Galanakis, Ph Mavropoulos, and Ph H Dederichs. Electronic structure and Slater–Pauling behaviour in half-metallic Heusler alloys calculated from first principles. *Journal of Physics D: Applied Physics*, 39(5):765, 2006.

[67] S Picozzi, AJFA Continenza, and Arthur J Freeman. Role of structural defects on the half-metallic character of Co2MnGe and Co2MnSi Heusler alloys. *Physical Review B*, 69(9):094423, 2004.

[68] A Candan, G Uğur, Z Charifi, H Baaziz, and MR Ellialtıoğlu. Electronic structure and vibrational properties in cobalt-based full-Heusler compounds: A first principle study of Co2MnX (X= Si, Ge, Al, Ga). *Journal of Alloys and Compounds*, 560:215–222, 2013.

[69] Hem Chandra Kandpal, Gerhard H Fecher, Claudia Felser, and Gerd Schönhense. Correlation in the transition-metal-based Heusler compounds Co2MnSi and Co2FeSi. *Physical Review B*, 73(9):094422, 2006.

[70] MP Raphael, B Ravel, Q Huang, MA Willard, SF Cheng, BN Das, RM Stroud, KM Bussmann, JH Claassen, and VG Harris. Presence of antisite disorder and its characterization in the predicted half-metal Co2MnSi. *Physical Review B*, 66(10):104429, 2002.

[71] WH Wang, M Przybylski, W Kuch, LI Chelaru, J Wang, YF Lu, J Barthel, HL Meyerheim, and J Kirschner. Magnetic properties and spin polarization of Co2MnSi Heusler alloy thin films epitaxially grown on GaAs (001). *Physical Review B*, 71(14):144416, 2005.

[72] Lance Ritchie, Gang Xiao, Yi Ji, TY Chen, CL Chien, Ming Zhang, Jinglan Chen, Zhuhong Liu, Guangheng Wu, and XX Zhang. Magnetic, structural, and transport properties of the Heusler alloys $Co_2MnSiandNiMnSb. PhysicalReviewB, 68(10) : 104430, 2003.$

[73] B Ravel, MP Raphael, VG Harris, and Q Huang. EXAFS and neutron diffraction study of the Heusler alloy Co2MnSi. *Physical Review B*, 65(18):184431, 2002.

[74] TD Haynes, RJ Watts, J Laverock, Zs Major, MA Alam, JW Taylor, JA Duffy, and SB Dugdale. Positron annihilation study of the Fermi surface of Ni2MnGa. *New Journal of Physics*, 14(3):035020, 2012.

[75] G Kontrym-Sznajd and M Samsel-Czekała. New reconstruction method of electron momentum densities from Compton profiles. *Applied Physics A*, 70(1):89–92, 2000.

[76] Percy W Bridgman. Certain physical properties of single crystals of tungsten, antimony, bismuth, tellurium, cadmium, zinc, and tin. In *Proceedings of the American Academy of Arts and Sciences*, volume 60, pages 305–383. JSTOR, 1925.

[77] Arthur H Compton. A quantum theory of the scattering of X-rays by light elements. *Physical review*, 21(5):483, 1923.

[78] Malcom J Cooper. Compton scattering and electron momentum determination. *Reports on Progress in Physics*, 48(4):415, 1985.

[79] DG Lock, VHC Crisp, and RN West. Positron annihilation and fermi surface studies: a new approach. *Journal of Physics F: Metal Physics*, 3(3):561, 1973.

[80] G Kontrym-Sznajd, A Jura, and M Samsel-Czekała. Special directions in the Brillouin zone. *Applied Physics A*, 74(5):605–612, 2002.

[81] John P Perdew. Jp perdew and y. wang, phys. rev. b 45, 13244 (1992). *Phys. Rev. B*, 45:13244, 1992.

[82] S Amari, R Mebsout, S Méçabih, B Abbar, and B Bouhafs. Correlation effects on the electronic structure of Co2Mn0.5Fe0.5Si and Co2Mn0.5Gd0.5Si quaternary alloys. *Intermetallics*, 37:27–31, 2013.

[83] Hem C Kandpal, Gerhard H Fecher, and Claudia Felser. Calculated electronic and magnetic properties of the half-metallic, transition metal based heusler compounds. *Journal of Physics D: Applied Physics*, 40(6):1507, 2007.

[84] Liviu Chioncel, Yuya Sakuraba, Enrico Arrigoni, MI Katsnelson, M Oogane, Y Ando, T Miyazaki, Emil Burzo, and AI Lichtenstein. Nonquasiparticle states in co 2 mnsi evidenced through magnetic tunnel junction spectroscopy measurements. *Physical review letters*, 100(8):086402, 2008.

[85] Adrian Stan, Nils Erik Dahlen, and Robert Van Leeuwen. Levels of self-consistency in the gw approximation. *The Journal of chemical physics*, 130(11):114105, 2009.

[86] Arno Schindlmayr. Violation of particle number conservation in the gw approximation. *Physical review B*, 56(7):3528, 1997.